Investigation of Discrete Flame Propagation Regime in Particulate Suspensions

Alex Wright

Master of Engineering

Mechanical Engineering

McGill University

Montréal, Québec

2015-08-15

This thesis is submitted to McGill University in partial fulfillment of the requirements for the degree of Master of Engineering

ACKNOWLEDGEMENTS

First and foremost, I would like to thank my supervisor, Andrew Higgins, for his wisdom and guidance throughout this project. This work could also not have been done without the support and advice from fellow members of the Metal Flames group, especially Sam Goroshin, along with my fellow graduate students Philippe Julien, Mike Soo, Jan Palecka, James Vickery, and Sam Whiteley. Professors Jeffrey Bergthorson and David Frost were also of great help during my time in this group. Finally, I'd like to thank my parents for their continued support and encouragement.

ABSTRACT

Suspensions of solid metal powders burning in a gaseous oxidizer can be modelled as a reaction-diffusion wave propagating through a heterogeneous mixture with discrete energetic sources. This is in contrast with more conventional models of flame propagation in areas such as gas combustion, where the reaction front and heat release profiles are homogenized continuous features. Under certain conditions the spatial dependence of the source term becomes important, and may affect the behaviour of the flame. This so-called discrete regime has lacked sufficient experimental verification. The present thesis discusses microgravity-based experiments that were performed, and introduces new lab-based experimental techniques for observing flames propagating in this discrete regime. Flame speed measurements corroborated the theoretical predictions, namely, an independence of flame speed upon oxygen concentration. Instabilities associated with metal dust flames were also investigated. Another fundamental property of solid fuels is their particle burn time. This parameter is important for determining the discreetness of a mixture, and supporting experiments were performed to determine the burning time of micron-sized iron powder particles. It was seen that the combustion process can terminate with either gradual burnout or premature explosion, depending on composition. The burn time results showed qualitative agreement with theoretical predictions. This work will support experiments on a sounding rocket microgravity platform scheduled for launch in 2016.

ABRÉGÉ

La combustion de suspensions de poudres métalliques dans un oxyde gazeux peut être représentée par la propagation d'un système à réaction-diffusion dans des mélanges hétérogènes de sources d'énergie discrètes. Ceci contraste avec les modèles plus conventionnels de combustion de gaz où le front de réaction et les profiles de libération de chaleur sont continus et homogénéisés. Sous certaines conditions, les variations spatiales de source deviennent importantes et peuvent affecter la flamme. Ce régime soi-disant discret manquait de vérification expérimentale suffisante. Cette thèse présente les expériences menées en microgravité ainsi que les nouvelles techniques expérimentales de laboratoire pour observer la propagation des flammes discrètes. Les mesures de vitesse de flamme corroborent les prédictions théoriques, en particulier, une indépendance sur la concentration en oxygène. Les instabilités associées aux flammes de poudres métalliques ont également été étudiées. Un autre paramètre fondamental des carburants solides, le temps de combustion de leur particules, est important pour étudier la nature discrète du mélange et a été déterminé par des expériences avec des particules microniques de fer. Le procès peut se terminer soit avec une combustion graduelle ou une explosion prématurée de la particule, suivant la composition. Ces résultats sont qualitativement en accord avec les prédictions théoriques. Ce travail supportera les expériences menées en microgravité à bord d'une fusée-sonde en 2016.

TABLE OF CONTENTS

LIST OF TABLES

LIST OF FIGURES

CHAPTER 1
Introduction

1.1 Overview of Metal Combustion

The study of metal powder combustion is an important area of research with relevance in numerous fields. The high energy of metals can be comparable to conventional fuels, such as gasoline or diesel, and on a volumetric basis they can be more energy dense than liquid hydrogen or propane. This high energy density makes the use of metal powders attractive in applications, including propellants and explosives; and as an energy carrier.[30, 56, 23, 22]

Propellants often use aluminum powder as their primary constituent. The solid rocket boosters used in the space shuttle contain 16% aluminum by weight, and the Japanese SRB-A solid rocket motor contains 18% aluminum. Recent research has also looked at combining nanoaluminum powder and water in a frozen slurry to create a propellant known as ALICE, for Aluminum Ice. Magnesium has also been proposed as a propellant for missions to Mars, as magnesium can burn using CO_2 as the oxidizer, which is the primary component of the Martian atmosphere.[54, 23] Boron has the highest volumetric energy density in reaction with oxygen as compared to any other element, and this has stimulated a large body of work investigating the use of boron for propulsion. It has been studied when both mixed with other fuels or when burned directly, however the oxide produced during boron combustion has prevented effective use as a fuel.[41] The

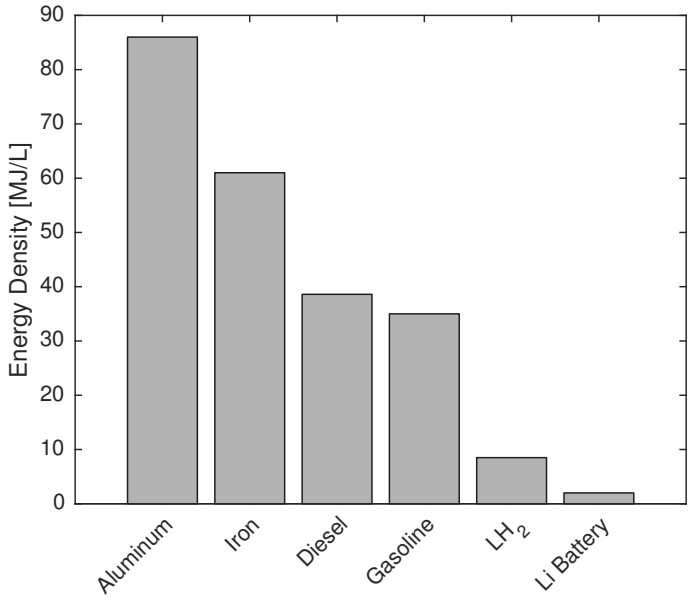

Figure 1–1: Volumetric energy densities of different materials.

high energy density of these metals also allows them to be used in explosives, where they can increase the blast intensity.

Another recent development has focused on using metal powders as an energy carrier, serving as a carbon-free alternative to conventional fuels. The energy from these metal powders can be harnessed either by direct combustion, or by reacting the metals with water to create hydrogen in a reactor. The oxide can then be collected and reprocessed using green energy solutions, such as wind or hydro power, producing a zero-emissions energy carrier.[3, 8]

The high energy density and reactivity of these metals also makes them relevant in an industrial safety context. Large suspensions of metal powders can be found in many industrial environments, and unintended ignition of these suspensions can result in destructive consequences. In recent years, there have

been numerous industrial explosions linked to the ignition of metal dust clouds.[17, 67]

Metal powders are also used in a process known as self-propagating high-temperature synthesis, or SHS. In this process, exothermic reaction waves travel through admixtures of condensed-phase reactants.[40] SHS is commonly used for the production of refractory materials with unique thermal, mechanical, or electrical material properties.[33] Metals such as aluminum, magnesium, titanium, and boron are often reacted with other compounds such as carbon or sulphur. Thermite reactions between metals and metal oxides are another type of combustion synthesis that has been used in pyrotechnic devices requiring extremely high temperature reactions.[21]

The combustion of suspensions of metal powders has been studied extensively since the 1950s using both experimental and theoretical approaches. Experimental techniques for studying suspensions of metal powders have included flames in tubes, stabilized Bunsen-style and flat flames, flames through large-scale unconfined clouds, and spherically expanding flames through suspensions in both constant-volume dust bombs and constant-pressure enclosures. Each of these techniques allows for the testing of different experimental parameters, such as oxidizing environment, scale, ambient pressure and temperature, and reactant composition. The different techniques also permit the observation of different combustion characteristics, including burning velocities, flame temperatures, quenching distances, product compositions, and spectral responses.

1.2 Discrete Source Term Model

The propagation of reaction-diffusion fronts through heterogeneous media is encountered in a number of fields both within and outside of combustion. In addition to some of the discussed applications for metal powders such as propulsion, SHS systems, and explosion scenarios, similar analogs for reaction-diffusion fronts through multiphase fields can also be found in other areas. In biology, calcium waves propagate between receptors as a means of cellular signalling.[15, 32] In astrophysics, the spiral arms of galaxies are believed to be self-propagating waves of star formation. Each of these scenarios relies on the diffusion of heat or reactants between discrete, localized sources.

For heterogeneous combustion models, the traditional approach is to treat the reactive media as spatially uniform, and the particulate nature of the fuel is only reflected in the reaction rate law used. The thermal source (i.e., burning particles) are conceptually homogenized throughout the medium, and the heat release from these solid fuel particles is approximated as a spatially continuous function, disregarding the discrete nature of the reacting particles. The validity of this approach is dependent on the scale of the heterogeneities. If the sources of chemical energy release are highly concentrated, and the time scale for heat diffusion between sources is much larger than the particle reaction time, the flame front propagation is dominated by the spatial discreteness of the media, and models that use an averaging or homogenizing approach may result in an erroneous description of flame propagation. In this case, the characteristic width of the flame zone will be less than the spacing between particles, and a uniform

flame front can no longer be easily defined. For accurate modelling of propagation in the examples listed above, it may be necessary to take the spatial distribution of these reaction sources into account. The question of whether the spatial distribution of sources needs to be taken into account in flame propagation arises anytime a particulate fuel is encountered. Recognition of this regime of flame propagation as being separate from traditional heterogeneous combustion has led to the terminology "discrete combustion waves" and is the subject of a thorough review [44, 51]. In this work, the unique properties of flame propagation in the discrete regime, in comparison to more traditional continuous heterogeneous combustion, will be explored using suspensions of metal fuels in gaseous oxidizers.

The applicability of the discrete regime to a given mixture can be quantified with a non-dimensional combustion time τ_c,

$$\tau_c = \frac{t_r}{t_d} \tag{1.1}$$

where t_r is the source energy release time (or combustion time for a fuel particle), and t_d is the inter-particle heat diffusion time $t_d = l^2/\alpha$. The heat diffusion time is dependent on the spacing between particles, l, and the thermal diffusivity of the mixture, α. In the limit of widely spaced, fast reacting particles in a mixture with low thermal diffusivity, this discreteness parameter will be much less than unity, and the positions of the particles must be described explicitly in the model in order to correctly predict the behaviour of the flame. In the other limit of the reaction time being long in comparison to the inter-particle diffusion time, $\tau_c > 1$, the flame is locally thermally uniform and spatial averaging allows traditional,

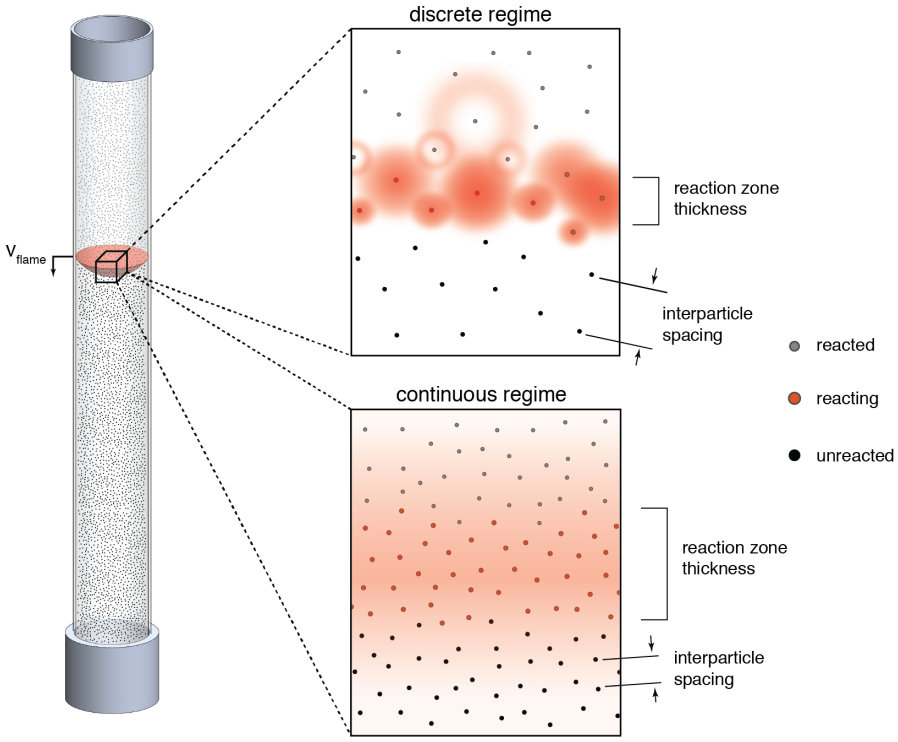

Figure 1–2: Schematic showing comparison between continuous and discrete regimes of combustion. In conventional continuous model of flame propagation, heat release is homogenized and smooth flame front is formed. In discrete model of flame propagation, flame behaviour is dictated by particle to particle heat transfer.

continuum-based models to be used. A schematic representation of the two different regimes is shown in Figure 1–2.

As a conceptually simple, illustrative model, the temperature field $\theta = T/T_{\mathrm{ad}}$, where T_{ad} is the adiabatic flame temperature, can be described by the reaction-diffusion equation for both the continuous and discrete regimes,

$$\frac{\mathrm{d}\theta}{\mathrm{d}\tau} = \nabla^2\theta + F \tag{1.2}$$

where the source term F expresses the nature of the source of heat via reaction. In the continuous case, the source term is defined as a step function that travels with the flame front

$$F = \begin{cases} 0 & \text{if } x < 0 \text{ or } x > \eta\tau_{\mathrm{c}} \\ \frac{1}{\tau_{\mathrm{c}}} & \text{if } 0 \leq x \leq \eta\tau_{\mathrm{c}} \end{cases} \tag{1.3}$$

An exact expression for front speed $\eta = \frac{vl}{\alpha}$ can be found by matching the solution for the preheat zone to the constant-heat-release reaction zone to obtain

$$\theta_{\mathrm{ign}} = \frac{1 - \exp(-\eta^2\tau_{\mathrm{c}})}{\eta^2\tau_{\mathrm{c}}} \tag{1.4}$$

where θ_{ign} is the ignition temperature non-dimensionalized by the adiabatic flame temperature and temperature of the unburned mixture, $\theta_{\mathrm{ign}} = \frac{T_{\mathrm{ign}} - T_{\mathrm{u}}}{T_{\mathrm{ad}} - T_{\mathrm{u}}}$. The ignition temperature can represent different mixtures or different concentrations of fuel. If this equation is linearized with the assumption that $\eta^2\tau_{\mathrm{c}} \ll 1$, it can be seen that the front speed η is inversely proportional to $\sqrt{\tau_{\mathrm{c}}}$. The front speed is limited only by the reaction rate of the particles, and as the reaction rate decreases towards zero, the front speed increases towards infinity.

In the discrete regime, the source term is described by δ-functions in space, reflecting the point-like nature of particles, and either a δ-function in time (for particles that release their heat effectively instantaneously) or step-functions in time (for finite particle combustion times). In this case, the source term takes the form

$$F = \begin{cases} \sum_{k=1}^{N} g(x)\delta(\tau - \tau_k) & \text{if } \tau_c = 0 \\ \sum_{k=1}^{N} \frac{1}{\tau_c} g(x) H(\tau - \tau_k) H(\tau - \tau_k - \tau_c) & \text{if } \tau_c > 0 \end{cases} \tag{1.5}$$

where the function $g(x) = 1$ if $x = x_k$ and 0 otherwise, and H is the Heaviside function. If the particles are distributed evenly in three-dimensional space, this problem can be solved analytically by the superposition of Green's functions to obtain an expression that implicitly defines the front speed

$$u(x) = \begin{cases} \frac{1}{(4\pi)^{3/2}} \sum_{m=1}^{\infty} \sum_{n=-\infty}^{\infty} \sum_{p=-\infty}^{\infty} \left(\frac{\eta}{m}\right)^{3/2} \exp\left(-\frac{(m^2+n^2+p^2)\eta}{4\tau}\right) & \text{if } \tau_c = 0 \\ \frac{1}{(4\pi\tau_c)^{3/2}} \sum_{m=1}^{\infty} \sum_{m=1}^{\infty} \sum_{m=1}^{\infty} \int_{(\frac{m}{n}-\tau_c)H(\frac{m}{n}-\tau_c)}^{\frac{m}{n}} \tau^{-3/2} \exp\left(-\frac{m^2+n^2+p^2}{4\tau}\right) \mathrm{d}\tau & \text{if } \tau_c > 0 \end{cases} \tag{1.6}$$

The relationship between front speed η and combustion time τ_c is plotted in Figure 1–3 for two different values of θ_{ign} that are of interest for this study. For non-dimensional combustion times τ_c greater than unity, the front speed in the discrete regime converges to the same behaviour as in the continuous regime. For $\tau_c < 1$, there is an insensitivity of front speed on combustion time, a unique characteristic of the discrete regime. When the combustion time is below unity, the front speed is limited by particle-to-particle heat diffusion, rather than the particle combustion time, and this feature explains the independence of flame speed upon

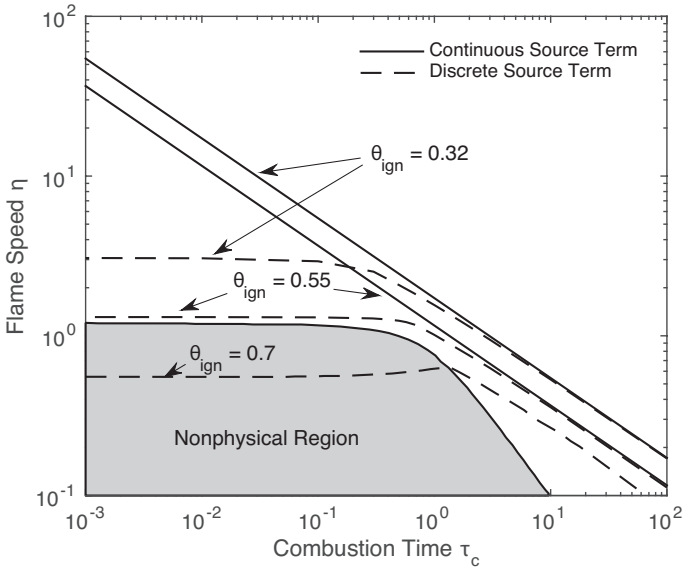

Figure 1–3: Nondimensional flame speed as a function of non dimensional particle combustion time for continuous and discrete models. Two different sets of curves are shown for different values of ignition temperature.

combustion time. In the definition for the discreteness parameter, the particle size will affect the particle spacing; however, if we assume a diffusively controlled burning mode, then the reaction time is proportional to the square of the particle diameter, $t_{\mathrm{r}} = Kd^2$, and these two effects negate each other, resulting in no net dependence on particle size.

The discrete regime of flame propagation was introduced by Goroshin et al. [25], where the model for front speed in a regular array of sources described above was first developed. At approximately the same time, a mathematically identical model was independently formulated for calcium signalling waves in cells by Keizer [32, 15, 42] that identified the same τ_{c} parameter as determining whether a continuum approach was valid or spatial discreteness must be taken

into account. More recent efforts have expanded upon these findings, including identifying a region of the ignition temperature/combustion time parameter space wherein the ignition of sources occurs under a nonphysical scenario of ignition in a decreasing temperature gradient.[5, 4, 62] If the constraint of a fixed period delay between sources is relaxed and dynamical solutions to the heat equation are instead used, flame propagation in this region is not possible (see shaded region in Figure 1–3). As flame propagation approaches this region, the flame dynamics becomes increasingly complex, exhibiting a cascade of period doublings in the delay time between source ignitions until the solution becomes chaotic and ultimately quenches.[5, 4, 62] This result, wherein a flame quenches in the absence of losses and at a finite flame speed, is believed to be unique in combustion theory, and is attributed to the spatially nonuniform structure of the flame.

In any real, experimental system, the sources of heat release will be randomly positioned in space, rather than in the regular arrays discussed above, and this feature results in substantially novel behaviour in the flame dynamics. The flame propagation under this scenario is now influenced by the inherent clustering that occurs when particles are randomly positioned, and the flame fronts in the discrete regime exhibit a roughened front structure. The overall qualitative behaviour of the flame speed, which approaches a plateau value as the nondimensional combustion time τ_c becomes less than unity as shown in Figure 1–3, is preserved. However, for the case of randomly positioned sources in two-dimensional simulations, flames in some simulations are able to continue propagation into the region of nonphysical ignition shown in Figure 1–3, where

propagation in regular arrays is not possible.[62, 28] In simulations of three dimensional clouds of randomly positioned sources, in some cases the flames are even able to propagate beyond the so-called thermodynamic limit $\theta_{\text{ign}} > 1$, defined by the condition where the ignition temperature exceeds the adiabatic flame temperature, by exploiting a percolation-like mechanism of propagation.[63] The flame propagation will follow a path of locally sufficient concentration, despite the global average concentration being above the thermodynamic limit. All of these results reflect the inherently statistical nature of flame propagation occurring in suspensions of condensed-phase sources in gaseous oxidizer. Such behaviour is not observed in laminar flame propagation in gases because fluctuations in gases occur on a mean free path scale that is many orders of magnitude smaller than the flame thickness, and thus can be safely neglected. This behaviour is distinct from the percolation-like propagation of laminar flamelets that occurs in non-premixed turbulent combustion, for which the scale of randomness is much larger than the flame thickness.[48] In the present case, significant particle clustering on a length scale comparable to the flame thickness itself is an inherent property of the media. The computational simulations of Tang [62, 63] suggest that local fluctuations in particulate distribution at this scale may profoundly alter the flame propagation dynamics, necessitating the introduction of concepts from statistical physics into combustion theory.

The discrete-source-term model predicts that in the limit of small combustion times, there should be an invariance of flame speed with reaction time (Figure 1–3). This is in contrast to the continuous model, where the flame speed

is approximately inversely proportional to the square root of the reaction time. In order to confirm these predictions, the flame speeds of different mixtures will be tested at increasing oxygen concentrations. The reaction time of a particle is inversely proportional to the oxygen concentration, and so in the discrete regime there should be no change in flame speed with increasing oxygen concentration, while the continuous regime should see an increase in flame speed with oxygen concentration. These tests are performed in fuel lean conditions, to ensure that the increasing oxygen concentration does not affect the thermodynamics of the flame. Some results in fuel rich conditions are presented as well, in order to show instabilities that arise in rich dust flames.

1.3 Metal Combustion in Microgravity

Experimental evidence for the discrete regime is difficult to obtain due to technical challenges inherent to flames in particulate suspensions (i.e., dust flames). Uniform suspensions of quiescent particles, particularly with the large particle sizes that better allow for observation of the flame structure, are difficult to create under normal gravity conditions due to particle settling. Settling particles can also form turbulent recirculation cells that will inhibit laminar flame propagation.[39] To overcome these problems, there has been a traditional motivation to perform dust combustion experiments in microgravity.[2, 16, 29, 52] An extensive program of using parabolic flight aircraft to investigate fundamental parameters of dust flame propagation (e.g., laminar burning velocity, quenching distances) has been undertaken at McGill for the last two decades.[61, 29, 60] Most of these studies examined flame propagation in the continuum regime.[61, 60]

By their nature, attempts at observing flame propagation in the discrete regime necessitate performing experiments under conditions of low fuel concentration, fast burning fuels, and low diffusivity media. These conditions often result in the flames propagating at low speeds that make them susceptible to buoyancy-induced convective flows that disrupt the flame. Buoyancy-driven convective flows scale with the body-force term (gravity) to the one third power ($g^{1/3}$).[52] Thus, to reduce buoyancy to the level where a flame propagation on the order of 1 cm/s might be observed, the apparent gravity would need to be reduced to below 10^{-3} g. Parabolic flight aircraft typically experience low-frequency g-jitter values of the order of 5×10^{-2} g or greater. The barrier to low speed flame propagation can be overcome by utilizing a high-quality microgravity environment.

An additional requirement for microgravity stems from the requirement of a uniform and well-quantified suspension of particulates. In a gravitational field, the settling of dust results in complex flows (convective cells) that can disrupt flame propagation.[39] The use of microgravity allows the suspension of large (up to 40 μm) particles, while ground-based experiments are usually limited to particles on the order of 5 μm. While, in principle, the discreteness parameter of a particular suspension can be shown to be independent of particle size (i.e., larger particles are more widely spaced to maintain the global concentration, but greater combustion time of the larger particles is proportional to the greater time for diffusion between particles, such that τ_c remains constant), experimentally the use of larger particles allows direct visualization of the particles in the suspension, and lower flame speeds allow for better observation of the flame structure.

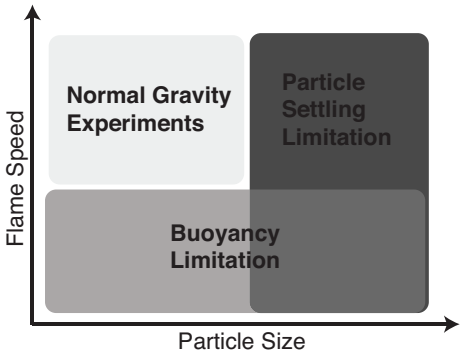

Figure 1–4: Demonstration of limited test envelope under normal gravity conditions.

Preliminary experimental evidence of flame propagation in the discrete regime was obtained by using iron particles in suspensions in gaseous oxygen heavily diluted with low thermal diffusivity xenon (with similar experiments using high diffusivity helium for the control case) on board a parabolic flight aircraft.[28] An independence of flame speed upon oxygen concentration was observed in the xenon-diluted mixtures. These experiments, however, suffered from the limited test time (22-24 s) and significant g-jitters (± 0.05 g) inherent to parabolic flight aircraft. For these reasons, a sounding rocket experiment (PerWaves onboard the Maxus-9 sounding rocket) targeted at experimental observation of the discrete flame propagation regime in particulate suspensions in the microgravity environment is in preparation by the European Space Agency and is scheduled to be launched in 2016. The expense and difficulty associated with microgravity research limits the scope of these experimental studies, and so the present thesis is motivated as a laboratory-based investigation for diagnostics development and preliminary validation of the discrete regime of flame propagation.

1.4 Single Particle Metal Combustion

The burning time and ignition temperature of single particles are important fundamental measurements for many heterogeneous combustion models. To facilitate experimental verification of this discrete theory, accurate measurements of the combustion time and ignition temperature of individual particles are critical.

For single magnesium particle combustion, there is a large amount of experimental literature data. The first single magnesium particle experiments were conducted in the early 1960's by Cassel [11, 12], where particles were ignited using a hot furnace. Other studies involving the ignition of single magnesium particles with hot gases include Prachukho [49], Shevtsov [57], Shafirovich [55, 54], and Valov [64, 65]. Other studies have looked at single magnesium particle combustion by igniting the particles with a pulsed laser, including work by Liebman [37], Law [34], and Legrand [36, 35]. A final common apparatus ignites particles behind a reflected shock wave in a shock tube, as seen in work by Boiko [9] and Roberts [50].

For single particle aluminum combustion, a similarly large body of work can be found in the literature, and is the focus of an extensive review by Beckstead.[7] The experiments for aluminum generally follow the same experimental procedures as for magnesium particles, however the higher ignition temperature requirements of aluminum particles makes pulsed laser and shock ignition experiments more common. Both the aluminum and magnesium experiments measure properties, such as burn times, ignition temperatures, and ignition delay, and correlate them with parameters such as particle diameter, oxidizer composition, ambient

pressure, and ambient temperature. Diagnostics include streak photography, schlieren techniques, high-speed filming, photomultiplier tubes, spectroscopy, cinemicrography, electron micrography, and thermocouples.

These large bodies of work exist for the single particle burning times for aluminum and magnesium; however, for other metals, such as iron, properties are not well documented. The limited experimental data available focuses on the combustion of iron particles in dense clouds.[59] In many cases, previous experimental techniques also have inherent limitations, such as overdriving particle ignition.[38, 36, 35, 37] The few existing empirical sources focus on a limited range of experimental parameters for particle size and oxidizing environment. Knowing the burning time and ignition temperature in the same environments in which supporting experiments are performed is critical for validating the theory being tested. In order to independently verify these parameters, a single particle burner apparatus was constructed.

Certain properties of iron make it an attractive metal when studying the burning times of particles. The Glassman criterion for the vapour phase combustion of materials states that for a particle to burn in the vapour phase, its oxide volatilization temperature must be greater than the metal's boiling temperature.[18] In this case, the fuel will vaporize and diffuse towards the oxidizing environment to react in the gas phase, while thermal diffusion to the particle surface sustains fuel vaporization. Iron is non-volatile, its adiabatic flame temperature (2250 K in air) is below its boiling temperature (3130 K), and there are no intermediate gaseous sub-oxides produced during the combustion process.[60]

Thus, the combustion reaction occurs heterogeneously on the surface of the particle, and produces only condensed-phase oxides. This simplifies the theoretical modelling of the combustion process. In contrast, aluminum and magnesium have oxide volatilization temperatures above their boiling points, and will react in the vapour phase.[18, 52]

It has been shown that the combustion of iron particles can be limited either by the rate of chemical reaction kinetics or by the rate of oxygen diffusion to the surface of the particle.[52] In the case of kinetically controlled burning, the burn time is proportional to the particle diameter,

$$t_{\mathrm{b,kin}} = \frac{\rho_{\mathrm{s}} d_0}{2 i \rho m_{0\infty} k_{\mathrm{s}}}, \tag{1.7}$$

where ρ_{s} is the particle density, d_0 is the particle diameter, i is the mass stoichiometric index, $m_{0\infty}$ is the mass fraction of oxygen, and k_{s} is the kinetic rate constant.[18]

For particles that burn in the diffusion-controlled mode, the burn time is proportional to the square of the particle diameter,

$$t_{\mathrm{b,diff}} = \frac{\rho_{\mathrm{s}} d_0^2}{8 \rho D \ln\left(1 + i m_{0\infty}\right)}, \tag{1.8}$$

where ρ and D are the density and diffusivity of the gas [18]. This simple model is based on the classical d^2 burning rate law used for droplets, and was extended to the diffusely controlled burning of metal particles with heterogeneous surface reactions by Glassman and Yetter.

Determining what will limit the particle combustion rate depends on the oxidizing environment and the particle size. This can be quantified by the Damköhler number,

$$\mathrm{Da} = \frac{t_{\mathrm{b,diff}}}{t_{\mathrm{b,kin}}} = \frac{d_0 i m_{0\infty} k_{\mathrm{s}}}{4D \ln\left(i m_{0\infty}\right)} \tag{1.9}$$

For Damköhler numbers much above unity, the combustion process will be primarily diffusion limited. This is the case with increasing particle size, large kinetic rates, low mass diffusivity, and low oxygen concentrations. In the opposite extremes, with Damköher numbers much below unity, the combustion process will be kinetically limited. In this case the diffusion of oxygen towards the particle will be much faster than the kinetics of the reaction.

CHAPTER 2
Laboratory Flame Propagation Experiments

2.1 Top-Down Magnesium Experiments

2.1.1 Motivation

The setup described in this section aimed to provide a laboratory apparatus that could be used to observe discrete flame propagation under normal gravity conditions. A top-down dispersion device was designed to allow for the dispersion of large sized particles (between 15 and 80 μm in diameter). If dispersed from below, particles in this size range would settle before they were properly dispersed. The larger sized particles afforded with a top-down design allows for better visualization of the flame front, as it can allow individual particles to be discerned.

2.1.2 Apparatus

The apparatus is composed of a dispersion device at the top, followed by a vertical glass tube in which the flame propagates, and finally a collection container and ventilation system at the bottom. The powder-feeding device sits at the top of the apparatus and consists of a bottomless hopper sitting on a rotating glass disk. The hopper has a small slit on the side in the direction that the disk rotates. The disk is coupled to an electric motor that allows it to rotate at variable speed. As the disk rotates, it carries a line of powder through the slit towards a stopping plate. As the powder reaches the plate, it is directed off the disk and into the flow ejector. The ejector allows the introduction of gas mixtures into

the combustion tube. From the ejector, the powder and gas mixture flow past a pneumatically controlled cutoff valve into a diffuser. The diffuser expands and laminarizes the flow into the combustion tube. The combustion tube is a glass tube 6 cm in diameter and 2 m long, with a secondary acrylic casing. At the base of the combustion tube is the ignition point. Ignition is achieved by passing high current through a tungsten wire suspended across the tube. The combustion tube finally leads to a collection box, which is connected to a central ventilation system. During operation, the powder flows downwards from the top of the tube and mixes with the gas introduced via the ejector to create a suspension of dust in the tube. Once the desired steady state concentration has been reached, ignition occurs simultaneously as the cutoff valve is activated, and a flame propagates upwards through the unburned metal fuel. The top of the tube is closed off to prevent the flame from accelerating upwards.

The diagnostics consist of high-speed cameras and a photomultiplier tube. The high-speed cameras include a Casio EX-F1 running at 300 fps for measuring flame speed, and a Photron Fastcam SA5 running at 5000 fps for observing the flame structure. The Sens-Tech P30A photomultiplier tube is used to discern individual particles igniting.

2.1.3 Metal Fuel and Gaseous Oxidizers

The discrete propagation mechanism requires a suspension of reactive particles that can act as point-like heat sources. These particles should be non-volatile, which prevents the use of organic dusts. Magnesium was initially chosen due to its high reactivity and availability. Spherical gran 16 magnesium was used, as

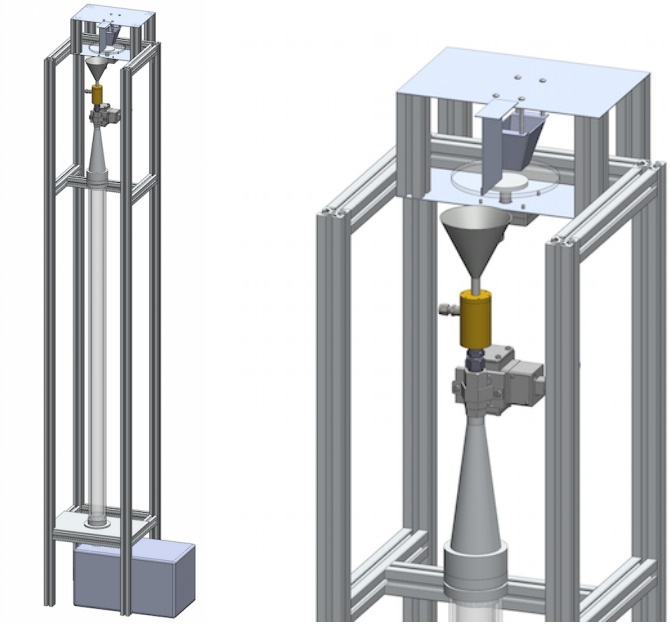

(a) Dimetric view of full apparatus.

(b) Detailed view of dispersion.

Figure 2–1: Model of top-down dispersion apparatus.

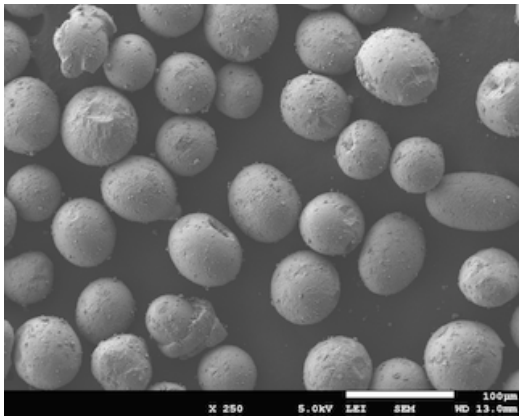

(a) SEM photo of 53-75 μm magnesium particles.

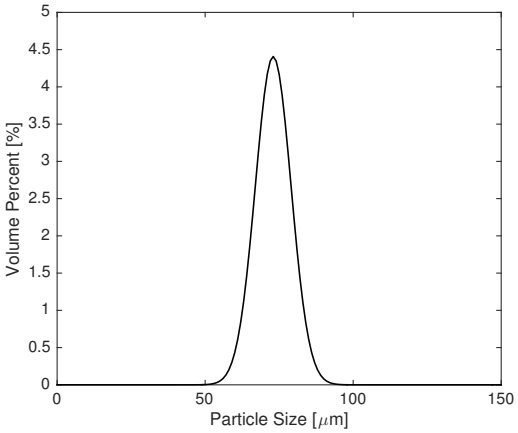

(b) Size distribution of 53-75 μm magnesium particles.

Figure 2–2: SEM and size distribution for magnesium powder tested.

shown in an SEM photo in Figure 2–2a. The powder was sieved into a series of tighter size distributions. The 53-75 μm cohort was chosen for initial tests, which had a Sauter mean diameter of $d_{3,2} = 71$ μm. The size distribution is seen in Figure 2–2b.

The oxidizer environment was achieved with in-line mixing of oxygen and nitrogen, controlled using rotameters. The oxygen concentration was verified using an oxygen analyzer. Mixtures were tested in oxygen concentrations of 21% and 75%, with nitrogen as the balance.

2.1.4 Determination of Discreteness Parameter

The burning time of a single magnesium particle in air with a diameter of 71 μm is 13.8 ms, as computed from the empirical relation found in [65]. For a suspension of these particles in air at a mass concentration of 300 g/m^3, the discreteness parameter can be calculated from the values in Table 2–1 to be

$\tau_c = 0.30$, which is much less than unity. The thermal diffusivity was taken at 300 K, and the average particle spacing is known from the fuel concentration. The burning time for magnesium burning in 75% oxygen is not available in the literature; however, it can be assumed that the burning time would only decrease, resulting in an even lower value for the discreteness parameter.

Table 2–1: Discreteness parameter for magnesium burning in air.

		Magnesium
Burning Time	t_r	13.8 ms
Thermal Diffusivity	α	22 mm^2/s
Particle Spacing	l	1.03 mm
Discreteness Parameter	τ_c	0.30

2.1.5 Preliminary Results

Measurements of flame speed were obtained by using a MATLAB script to track the location of the flame front over time from the high-speed videos. The slope of this curve gives a direct measurement of flame speed. The results of a typical flame speed measurement are shown in Figure 2–3a. This process was repeated for two trials in 21% oxygen and two trials in 75% oxygen. The results are shown in Figure 2–3b.

The photomultiplier was directed at a 4×4 cm^2 region of the tube in order to capture the light intensity over time with a high temporal resolution. The results seen in Figure 2–4 show discernible peaks corresponding to individual ignition events. This highlights the discrete nature of this fuel, where the flame propagation mechanism relies on discrete source reactions.

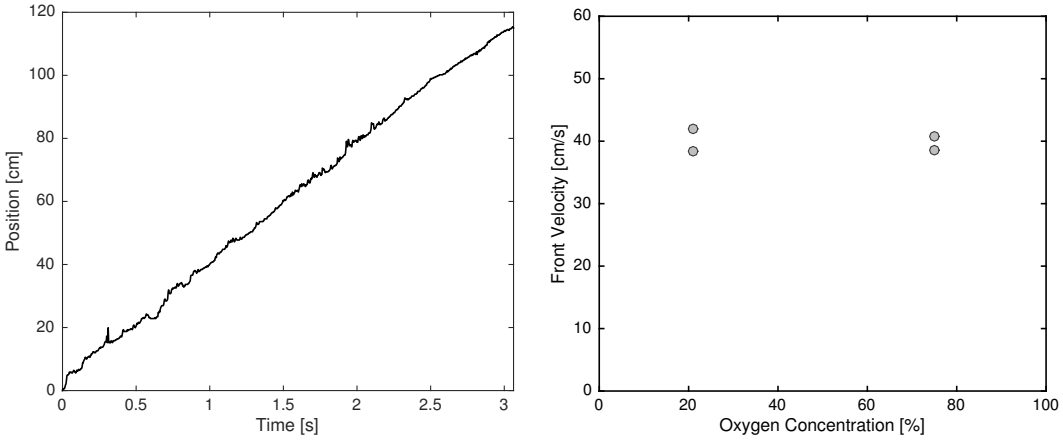

(a) Position tracking of flame. Slope gives measurement of flame speed.

(b) Flame speed measurements for magnesium powder.

Figure 2–3: Preliminary flame speed measurements in magnesium powder, averaged over entire length.

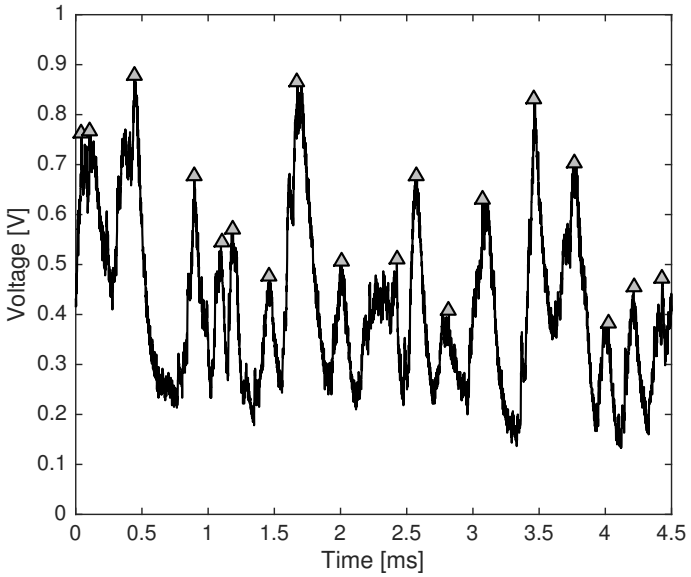

Figure 2–4: Photomultiplier trace of magnesium flame propagation. Peaks represent discrete, individual particles igniting.

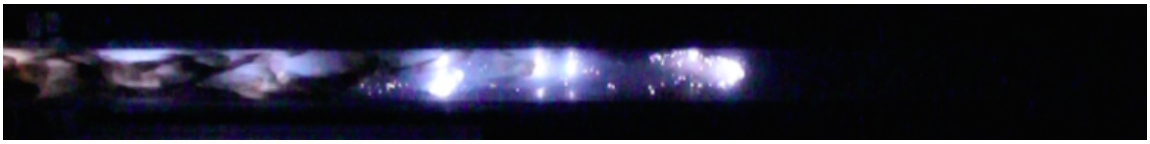

Figure 2–5: Picture of magnesium flame propagating upwards in a vertical tube. Image has been rotated so flame is propagating from the left to the right. Large sections of the tube can be seen burning simultaneously, beneath the flame front.

2.1.6 Problems

It was seen that the propagation of the flame upwards through the tube was often turbulent in nature, with a large area burning simultaneously. Unburned sections below the flame front would ignite after the flame front had already propagated past that section. This can be seen in Figure 2–5.

This turbulence indicated the likelihood of a non-uniform suspension. Laser sheet imaging was used to determine the uniformity of the dispersion. Observations showed that the flow appeared highly turbulent in nature, with large recirculation cells forming for the full length of the tube. Figure 2–6 shows the recirculation cells made visible during dispersion with a laser sheet.

It has been shown previously, both theoretically and experimentally, that these recirculation cells form when powder within the size range tested is dispersed downwards into a tube.[39] The falling of the particles induces recirculation cells inherent to the system.

2.2 Bottom-Up Aluminum and Iron Experiments

2.2.1 Motivation

In an effort to improve upon the problems created by the recirculation cells seen in the top-down dispersion apparatus, a similar apparatus originally

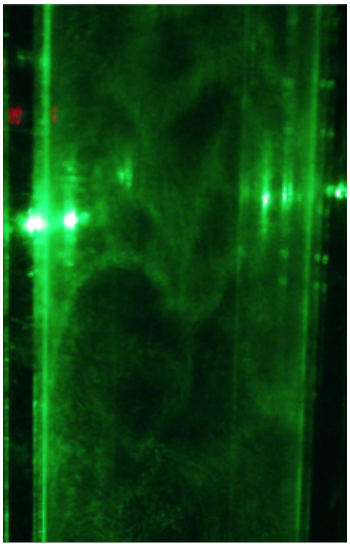

Figure 2–6: Frame from video of dispersion process with laser sheet illuminating axial plane of tube shows large recirculation cells.

devised for use in the microgravity environment on-board a parabolic aircraft was modified for use on the ground. This apparatus was rotated so it disperses from the bottom-up, and a smaller sized powder was used to allow for more quiescent mixtures. The small particles have a much lower Stokes velocity, and so will not create recirculation cells as they slowly settle. The powder was also changed from magnesium to aluminum, due to a lack of availability of smaller sized magnesium powders. The combustion time for aluminum particles is approximately two times longer than that of magnesium (as seen from calculations in Tables 2–1 and 2–3), however theoretical calculations show that lean mixtures of aluminum should still burn within the discrete regime. Laser sheet imaging confirms that the recirculation cells are no longer present with the bottom-up apparatus dispersal mechanism.

2.2.2 Apparatus Description

The apparatus used disperses a cloud of metal powder into a vertical glass tube 5 cm in diameter and 60 cm long using the gaseous oxidizer for each particular experiment. A longer tube (1.4 m) was also used in some tests to determine the influence of tube length on the results. Dispersion occurs from the bottom, and is achieved by actuating a piston that pushes a vertical column of packed metal powder upwards into the path of a inwardly flowing, sonic radial air knife. The gas mixture flowing through the air knife is the same gas that creates the oxidizing environment within the tube. The air knife deagglomerates and disperses the powder through a diffuser that makes the flow laminar as it moves upwards into the tube. During operation, powder flows upwards from the base of the tube until a steady state concentration is achieved. The top of the tube is open so that a steady flow of dispersed powder is exhausted prior to an experiment and also so that products can freely exhaust once the flame is ignited, maintaining constant pressure conditions. As the dust dispersion exits the tube, it passes through and attenuates a 5 mW, 632 nm laser beam that is focused onto a PDA-55 photodetector. The voltage drop measured by the receiver is correlated to a concentration measurement using a calibrated Beer-Lambert curve.[24] When a steady concentration is reached, ignition occurs at the top of the tube by passing a high current through a 20 μm diameter tungsten wire. The flow of gas from the air knife is stopped simultaneously with ignition, so that a flame travels downwards toward the closed end through the quiescent suspension of powder. The uniformity and lack of agglomeration in the powder suspension has been verified using a laser

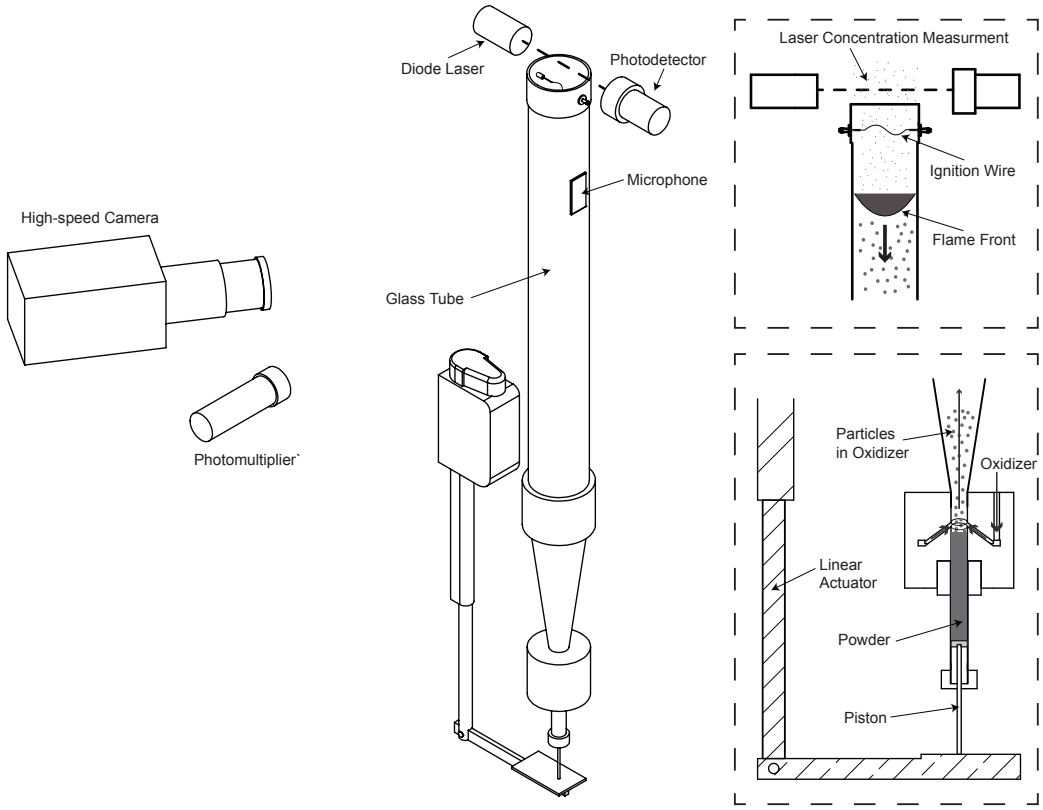

Figure 2–7: Schematic of bottom-up apparatus used for aluminum and iron trials.

sheet directed through the centre of the tube, illuminating a full-length axial cross section of the tube. Further details of the apparatus are described in [29].

Concentration Measurement

The concentration monitoring is performed with a laser-receiver pair positioned just above the exit of the tube. The powder passes through the horizontal beam, and the light intensity recorded by the photodetector is attenuated. A consequence of the Beer-Lambert law is that there will be a logarithmic relationship

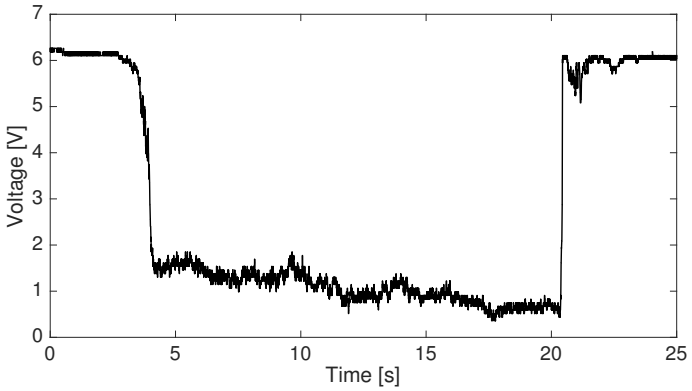

Figure 2–8: Trace of voltage attenuation by powder dispersion for concentration measurements.

between the voltage drop of the laser and the concentration,

$$m \cdot B = \ln\left(\frac{V_0}{V}\right) \tag{2.1}$$

where B is the concentration, V_0 is the unattenuated voltage level, V is the attenuated voltage level, and m is the scaling constant dependent on the optical properties of a particular powder.[24] The scaling constant was found for each powder by dispersing the powder at different concentrations, and after a steady state dispersion is reached, powder was collected into a filter over a known period of time. The mass of the powder collected over time can be divided by the flow rate measured with a flow meter to obtain a concentration measurement. The concentration obtained at each actuator speed was plotted against the natural log of the voltage drop, $\ln(\frac{V_0}{V})$, and the slope of this curve gives m. This calibration curve can be seen in Figure 2–9, and an example of the photodetector laser attenuation trace can be seen in Figure 2–8.

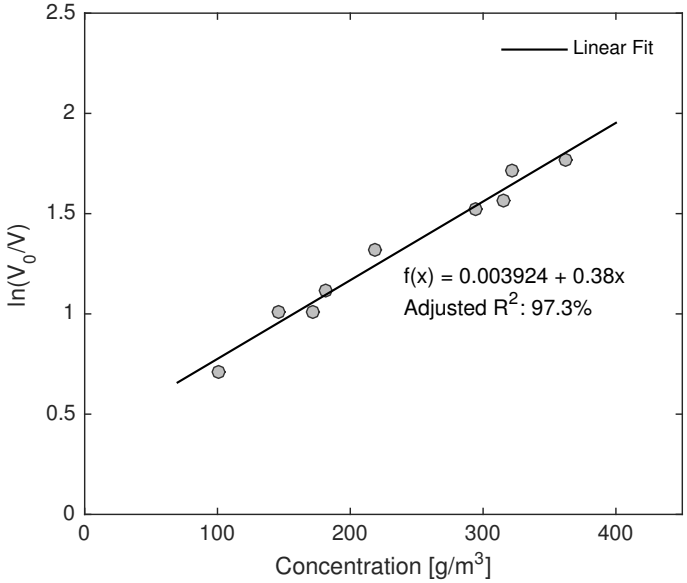

Figure 2–9: Laser calibration curve.

2.2.3 Metal Fuels and Gaseous Oxidizers

Three different metal powders were tested, two aluminum and one iron, with approximately similar particle sizes. The complete properties of the particles are given in Table 2–2. SEM photos of these powders are shown in Figure 2–10. Figure 2–10d shows the particle size distributions as determined by a Malvern Mastersizer 2000.

Table 2–2: Details of metal powders tested in bottom-up apparatus.

	Aluminum	Aluminum	Iron
Manufacturer Designation	Valimet H-5	Ampal 637	Alfa Aesar 98%
Sauter Mean Diameter	9.2 μm	6.5 μm	2.5 μm
Shape	Spherical	Irregular	Spherical

The experiments examining flame propagation in suspensions of these powders were conducted in an oxidizing environment with argon as the inert balance,

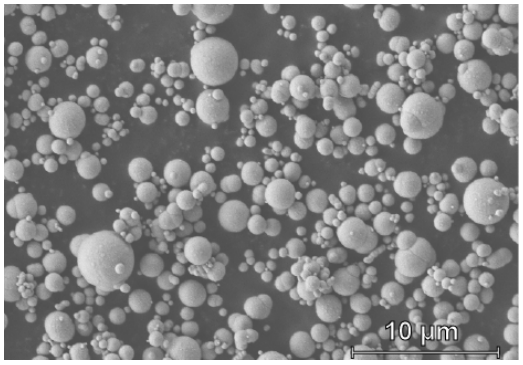

(a) Valimet H-5 Aluminum

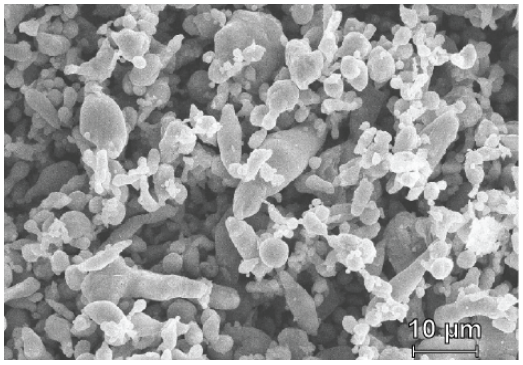

(b) Ampal 637 Aluminum

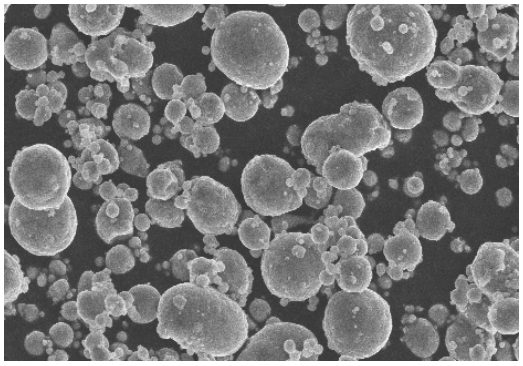

(c) Alfa Aesar 98% Iron

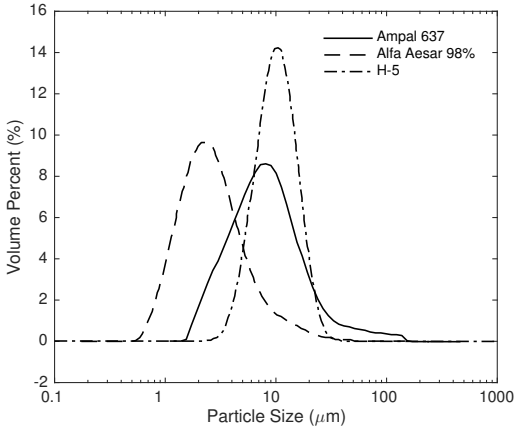

(d) Size distributions

Figure 2–10: SEM photos and Malvern Mastersizer 2000 size distributions for powders tested.

with the oxygen concentration varying from 15% to 60%. These mixtures were either commercially supplied and certified by Praxair to an accuracy of ±0.8%, or prepared by the method of partial pressure mixing in a reservoir at a total pressure of 14 bar, with an accuracy of ±0.7%. The prepared mixtures were allowed to mix for a period of at least 48 hours prior to use in an experiment, and the composition was verified with an oxygen analyzer.

2.2.4 Determination of Discreteness Parameter

In order to determine the regime of flame propagation for these experiments, the discreteness parameter τ_c must be calculated, which requires knowing the thermal diffusivity of the mixture, the particle spacing, and the estimated particle burning time. The estimated values of these parameters are given in Table 2–3. The thermal diffusivity was taken at 300 K, and does not change appreciably with varying oxygen concentration due to the similar thermal diffusivities of oxygen and argon. The average particle spacing is known from the fuel concentration.

The particle burning times for the iron powder were calculated using the classical d^2 law for diffusion limited combustion [18] assuming an oxidizing environment at 1000 K. Iron combustion does not involve gaseous sub-oxides and occurs entirely heterogeneously, on the surface of the iron particle.[60] Although the particle size range tested is likely in a transitional mode where it may also be partially kinetically limited, in this case a kinetically limited burning time would be greater than the diffusion limited burning time, and so the discreteness parameter would only increase. The particle spacing was calculated assuming a lean mass concentration of 600 g/m^3. For oxygen concentrations between 15

and 60%, the discreteness parameter of iron was calculated to be in the range $\tau_c \approx 3.1$–1.1 (see details in Table 2–3).

For aluminum, the burning times were calculated using Beckstead's empirical correlation based on the extensive analysis of the available experimental data.[7] Aluminum burns as a vapour cloud surrounding the partially volatilized aluminum droplet, resulting in shorter combustion times in comparison to iron. The particle spacing was calculated assuming a lean mass concentration of 250 g/m^3. This yields a discreteness parameter τ_c below unity for the oxygen ranges tested ($\tau_c < 0.6$).

Table 2–3: Discreteness parameters for powders tested in bottom-up apparatus.

		Aluminum	Aluminum	Iron
Manufacture Designation		Valimet H-5	Ampal 637	Alfa Aesar 98%
Oxygen Range		21–60%	15–30%	15–60%
Burning Time	t_r	0.48–0.16 ms	0.35–0.18 ms	0.32–0.11 ms
Thermal Diffusivity	α	22 mm^2/s	22 mm^2/s	22 mm^2/s
Particle Spacing	l	0.16 mm	0.12 mm	0.05 mm
Discreteness Parameter	τ_c	0.38–0.14	0.57–0.29	3.1–1.06

2.2.5 Initial Attempts

Experimental Details

Initial experiments with the bottom-up apparatus used the Valimet H-5 aluminum powder. This powder is spherical in shape, and has a Sauter mean diameter of 9.2 μm. This powder was tested in oxidizing environments of 21%, 42%, and 60% oxygen, with argon as the balance. Flame propagation was initially recorded with a Casio EX-F1 camera operating at 300 fps and a resolution

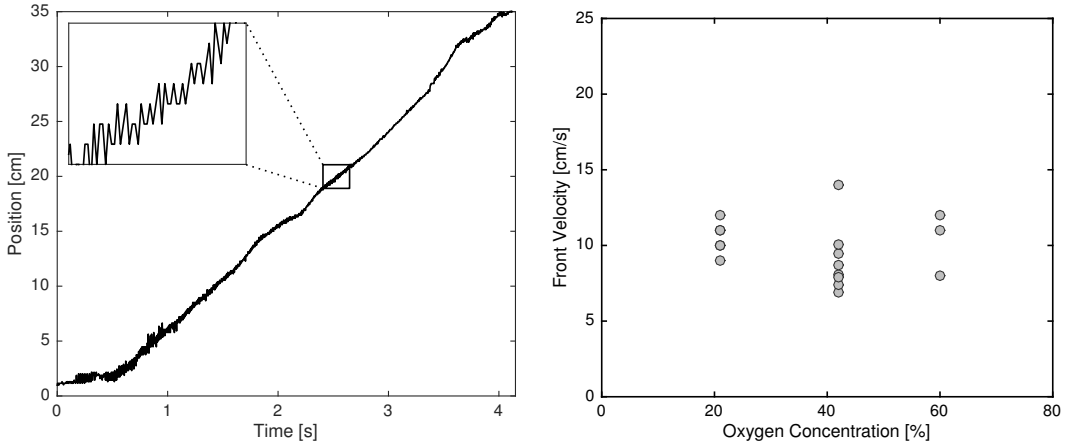

(a) Position tracking of flame showing existence of unstable regions.

(b) Flame speed measurements for Valimet H-5 aluminum.

Figure 2–11: Flame speed measurements in Valimet H-5 aluminum, averaged over entire length.

of 512×384 pixels. Tracking the position of the flame front over time gives a measurement of the flame speed.

Preliminary Results

This frame rate allowed for accurate measurements of flame speeds, however it was observed that there were pulsating oscillations at frequencies on the order of the framing rate of the camera. Due to the inability to accurately discern these regions, the flame speeds were obtained by averaging the slope across the entire length of the tube, including the regions where these pulsations occur. The results of this analysis are shown in Figure 2–11.

2.2.6 Improved Methodology

Experimental Details

The inability to accurately characterize these pulsating regions motivated the addition of improved diagnostics, including a high-speed Photron SA-5 camera operating at 2000 fps and a resolution of 1024×1024 pixels, a Sens-Tech P30A photomultiplier tube, and an electret microphone. The Photron SA-5 high-speed camera provides a visual representation of the pulsations, and the average flame intensities can provide a measurement of pulsation frequency. The photomultiplier tube provides a spatial average of light intensity with a high temporal resolution. The microphone attached to the tube provides an additional measure of the pressure waves produced by the pulsations. The aluminum powder selection was also changed from Valimet H-5 to Amapal 637, due to better dispersion properties and to allow for comparison with a number of previous experiments that have been performed.[26, 20, 19] Experiments were also performed with Alfa Aesar 98% iron, as a control for the continuous case.

Stable Propagation

Figure 2–12 shows the trajectory of the flame front obtained from processing the high-speed video of a flame propagating through a lean iron mixture (42% oxygen, 230 g/m^3). The resulting distance-time trajectory extracted from the video shows an initial ignition transient until 0.7 s, during which the flame gradually accelerates. After this point, the flame reaches a constant velocity and propagates steadily down the tube, as indicated by the constant slope in the

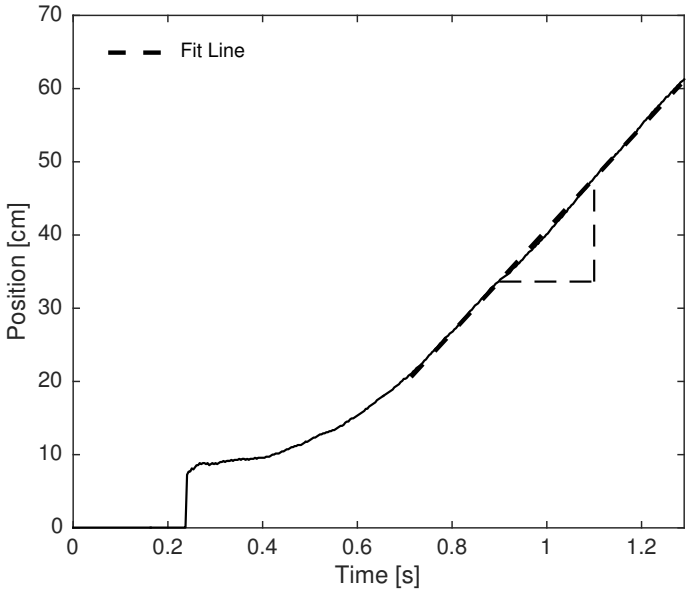

Figure 2–12: Position of flame front over time for a steadily propagating iron flame. The slope provides a measurement of flame speed.

position-time graph. The linear portion of this curve was fit using a line, and the slope provides a direct measurement of flame speed.

Instabilities

In addition to the technical difficulties associated with obtaining laminar flames in particulate suspensions under laboratory conditions, a number of the experiments conducted in this study exhibited evidence of instabilities. These instabilities did not always occur, and often repeated tests performed under as identical conditions as experimentally possible would exhibit both stable and unstable flames in the same region of the tube. A summary of the experimental observation of these instabilities is presented here. The nature of these instabilities will be explored further in Section 2.3.1.

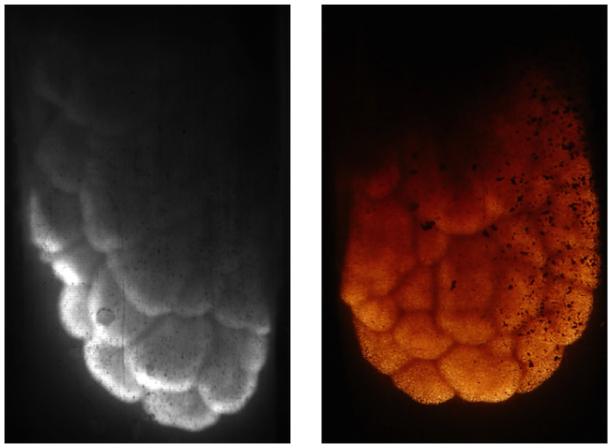

(a) Aluminum burning in ground-based apparatus.

(b) Iron burning in microgravity-based apparatus.

Figure 2–13: Cellular flames in rich aluminum and iron mixtures burning in 21% oxygen. Flames are propagating top to bottom.

Although the majority of this study was performed under lean conditions, select aluminum experiments were performed under rich conditions (21% oxygen, mass concentration above 500 g/m^3). A photograph of a flame front in this case is shown in Figure 2–13a, and is similar in appearance to the cellular flames observed in lean methane/air or rich propane/air mixtures. Rich iron flames were not tested in these sets of trials due to the increased stoichiometric concentrations required and the higher density of iron making it difficult to achieve rich flames under normal gravity conditions. Previous experiments in microgravity however have shown the same cellular structure in rich iron flames, as in Figure 2–13b. In the lean mixtures of aluminum used for the majority of this study, pulsating instabilities of the entire flame front were frequently observed. These instabilities did not occur in every trial, and they were often only seen in limited sections of

the tube. The occurrence of instabilities depended on the oxidizing environment, the metal fuel used, and the concentration of fuel. With the iron powder tested, the pulsations occurred rarely and only with high oxygen concentrations (greater than 42% oxygen). For the aluminum experiments, the pulsations occurred even at low oxygen concentrations (15% oxygen), however in these cases there are still sections of the tube where steady propagation could be observed and an average flame speed measurement taken. At high oxygen concentrations, however, the pulsations occurred for the full length of the tube, preventing measurements of a steady front velocity. This phenomenon limited the range of oxygen concentration that could be considered in the aluminum trials to a relatively narrow range of 15 to 30%, while the stability of the iron mixtures permitted tests between 15 and 60% oxygen concentration.

The observed pulsations consisted of both high frequency (230 to 350 Hz) oscillations that appeared to occur on the scale of the flame thickness and low frequency (100 to 150 Hz), large pulsations where the entire flame was periodically displaced in the axial direction on a scale much larger than the flame thickness. These are denoted high frequency and low frequency oscillations, respectively. In order to characterize these pulsating instabilities, different diagnostics were used. The low frequency pulsations occurred in virtually all aluminum trials, and select iron trials at high oxygen concentrations. The high frequency pulsations occurred only in select lean aluminum trials. The low frequency pulsations tended to occur around the midpoint of the tube, while the high frequency pulsations occurred closer to the top of the tube.

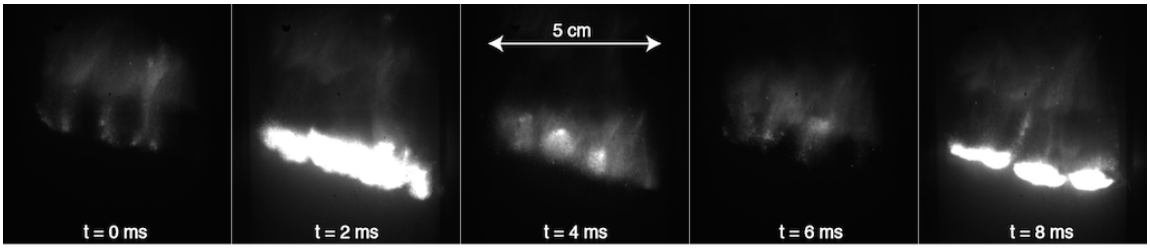

Figure 2–14: Low frequency, large amplitude pulsations seen in a rich aluminum mixture.

Figure 2–14 shows a sequence of high-speed video frames of the low frequency, large amplitude (greater than the flame thickness) pulsations seen in a rich (800 g/m^3) aluminum mixture burning in 21% oxygen and 79% argon.

Figure 2–15a shows pulsations seen in a lean mixture of aluminum (460 g/m^3 burning in 60% oxygen, 40% argon), captured using the different diagnostics. The frequencies captured by the high-speed camera, photomultiplier tube, and microphone are all in agreement. Figure 2–15b shows the frequency over time data from this trial. In this trial, the pulsations occurred part way into the propagation of the flame, and occurred for 0.5 s before dying out. The pulsations during this trial occurred at a relatively constant frequency around 105 Hz.

Figure 2–16a shows the frequency over time data for another aluminum trial (390 g/m^3 burning in 42% oxygen, 58% argon) where both the high frequency and low frequency pulsations were observed. This figure shows how the initial high frequency pulsations transition to a lower frequency pulsation part way down the length of the tube. Figure 2–16b shows a Fast Fourier Transform (FFT) of the amplitude over time data for the same trial, showing peaks at the two

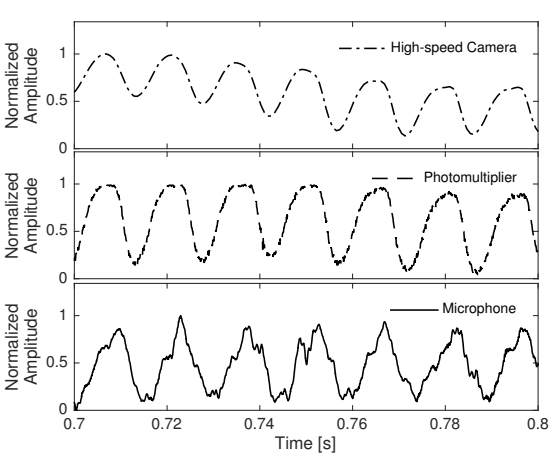

(a) Pulsations recorded by several diagnostics for lean aluminum mixture (460 g/m^3 burning in 60% oxygen, 40% argon).

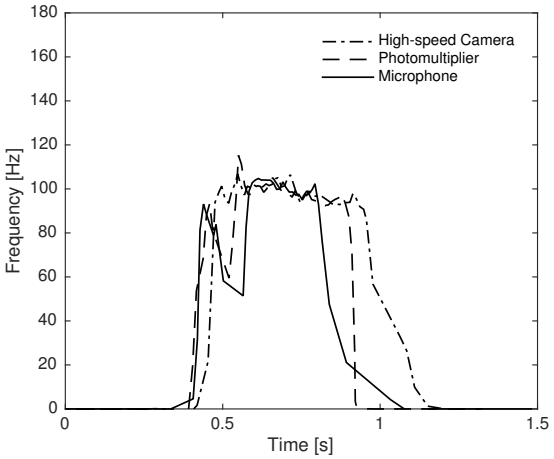

(b) Frequency over time results for low frequency pulsations seen in lean aluminum mixture (460 g/m^3 burning in 60% oxygen, 40% argon).

Figure 2–15: Low frequency pulsations seen in lean aluminum mixtures.

observed frequencies. The high sampling rate of the captured data relative to the frequencies observed prevents aliasing issues.

To better characterize the pulsation mechanism, limited trials were performed in a 1.4 m length tube, which is approximately twice as long as the tube in the earlier experiments (0.6 m). Trials were performed in 42% oxygen to ensure the occurrence of pulsations. These trials showed that the lower frequency, larger amplitude pulsations occurred at roughly half the frequency (50 to 70 Hz) as in the shorter, standard tube. Higher frequency pulsations between 100 and 350 Hz were also observed in the longer tube trials. A FFT of a single trial in this long tube can be seen in Figure 2–17a.

The complete sets of frequencies observed for all trials in both the short and longer tubes are compiled in Figure 2–17b. This figure shows the frequencies

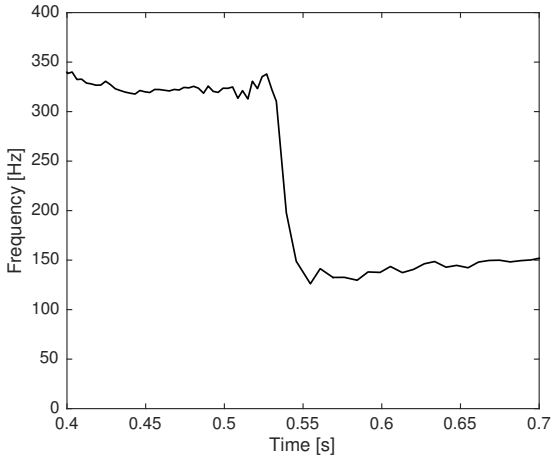

(a) Frequency over time data for lean aluminum trial (390 g/m^3 burning in 42% oxygen, 58% argon) with both high and low frequency pulsations, as captured by microphone.

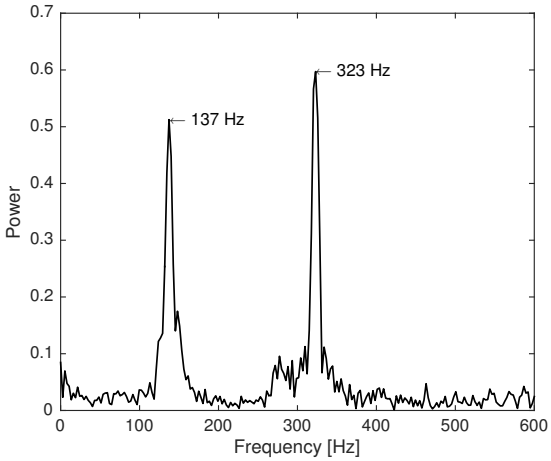

(b) FFT of amplitude over time data for lean aluminum trial (390 g/m^3 burning in 42% oxygen, 58% argon) with both high and low frequency pulsations, as captured by microphone.

Figure 2–16: High and low frequency pulsations observed in aluminum trial.

observed for all trials performed at each oxygen concentration. The frequencies appear to be grouped together, however due to the scatter in the data owing to the wide range of frequencies observed, there is no clear trend. The 15% oxygen case shows a maximum frequency observed of around 250 Hz, in contrast to the higher frequencies of around 350 Hz observed for the increased oxygen concentrations. Another noticeable behavior is that pulsations between 50 and 100 Hz are only observed in the longer (1.4 m) tube, while the lowest frequencies observed in the shorter (0.6 m) tube begin at 100 Hz.

Flame Speeds

Despite the complication created by the occurrence of pulsating flames described in the previous section, stable flame propagation could still be observed

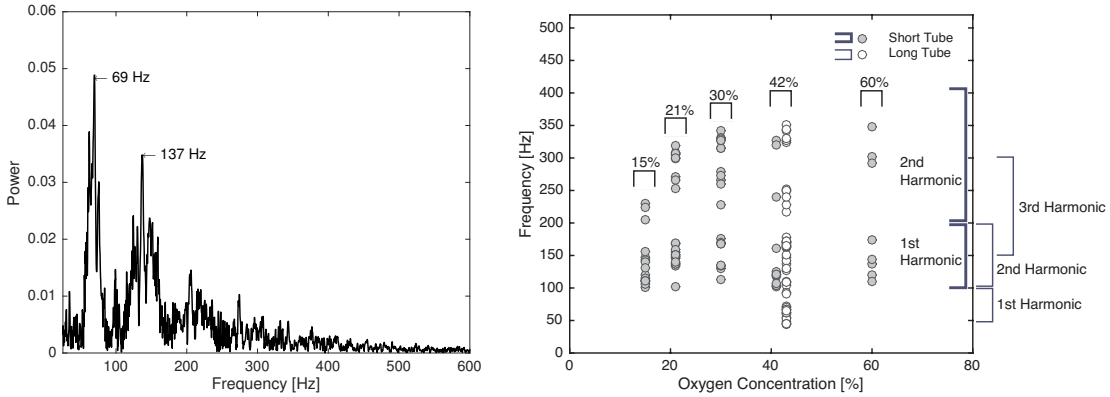

(a) FFT of amplitude over time data for lean aluminum trial in long tube with both high and low frequency pulsations, as captured by photomultiplier tube.

(b) Compilation of all frequencies observed in all aluminum trials performed, in both short and long tubes.

Figure 2–17: Frequencies observed for pulsations in tubes at different oxygen concentrations.

in iron suspensions over a range of oxygen concentrations from 15 to 60% and in aluminum suspensions from 15 to 30%. While pulsating oscillations were frequently encountered in aluminum suspensions, sufficiently long regions of stable propagation could be identified to permit accurate determination of flame speed. An example of this is shown in Figure 2–18, where a typical trace of the front trajectory over time for a lean aluminum flame is plotted. A flame speed measurement can only be taken from the initial steady region occurring in the first 25 cm of the tube.

For each iron suspension, an average of 5 repeated tests were performed at each oxygen concentration and the measured stable flame speeds were reported with each test shown as separate data points in Figure 2–19a. For aluminum

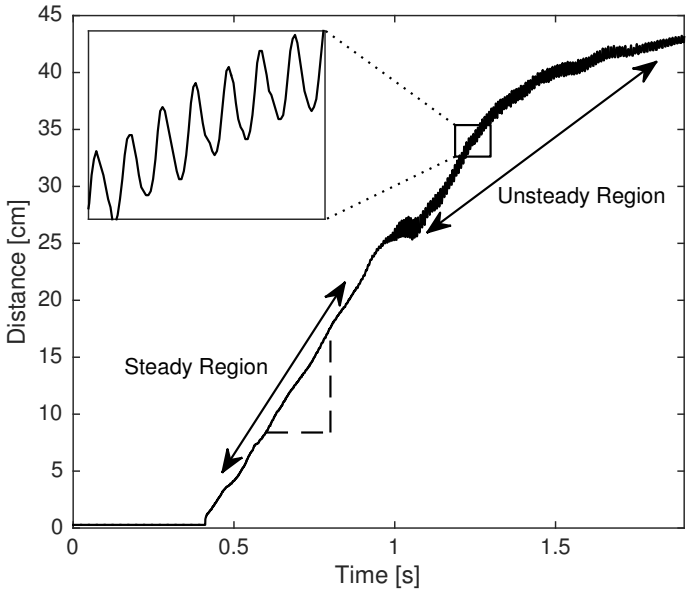

Figure 2–18: Tracking location of aluminum flame front over time shows steady regions where flame speed can be measured, and unsteady regions where pulsations occur.

suspensions, an average of 12 tests were repeated at each oxygen concentration, as shown in Figure 2–19b. The scatter in the data can be attributed primarily to local variations in dust concentration, which can have a direct impact on flame speed by affecting the thermodynamics of the flame, and also indirectly by changing the surface area of the flame front. The iron suspensions exhibit a monotonically increasing flame speed with increasing oxygen concentration, with the average flame speed increasing from 40 to 80 cm/s, while the aluminum suspensions, with an average flame speed of 45 cm/s, do not exhibit any significant correlation with oxygen concentration.

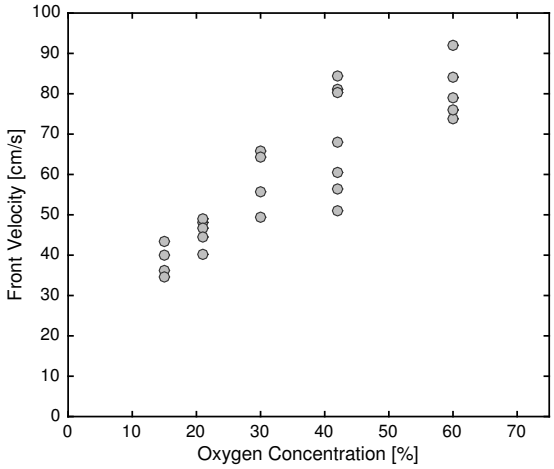

(a) Flame speeds of Alfa Aesar 98% iron at different oxygen concentrations

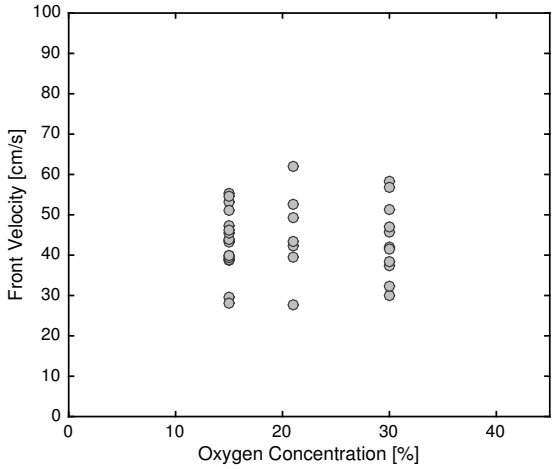

(b) Flame speeds of Ampal 637 aluminum at different oxygen concentrations

Figure 2–19: Measured flame speeds of iron and aluminum powders

2.3 Analysis

2.3.1 Instabilities

The occurrence of pulsating flame instabilities was an unexpected experimental outcome of this study, and was not the primary focus of the experiments; however, it is possible to attempt a preliminary interpretation of these results. The two mechanisms hypothesized to be responsible for the instabilities are thermo-diffusive and thermo-acoustic instabilities.

Thermo-diffusive flame instabilities can occur when the Lewis number of a mixture is much above or below unity.[33] Lewis numbers less than one can be readily achieved with premixed gases, however Lewis numbers much above unity are more difficult to realize.[47] For the heterogeneous combustion of metal powders, however, their unique properties make them susceptible to instabilities resulting from Lewis numbers both above and below unity.[45] The Lewis number

is defined as the ratio of the thermal diffusivity of the mixture to the mass diffusivity of the deficient reactant. For rich mixtures of metal powders in a gaseous oxidizer, the deficient reactant is the oxygen. The thermal diffusivity of the mixture will be reduced due to the increase in thermal mass of the mixture, while the mass diffusivity of oxygen remains constant. In this case,

$$\mathrm{Le} = \frac{\alpha}{(\rho_{\mathrm{g}} c_{p,\mathrm{g}} + B c_{p,\mathrm{s}}) D} \tag{2.2}$$

where ρ_{g} is the density of the gas, $c_{p,\mathrm{g}}$ is the specific heat capacity of the gas, B is the mass concentration of fuel, and $c_{p,\mathrm{s}}$ is the specific heat capacity of the fuel. For a typical rich aluminum flame with a concentration of 600 g/m^3, the Lewis number will be approximately 0.5. Under these conditions, it has been shown that cellular instabilities can form in gaseous mixtures.[33] This nonequidiffusional instability arises due to the mobility of the deficient reactant, which tends to intensify variations in flame curvature. This instability has been well documented for gaseous flames.

For lean mixtures of metal powders in a gaseous oxidizer, the deficient reactant is the metal fuel. Due to the practical lack of mass diffusivity of the particles, the Lewis number approaches infinity.[66] In this situation, it has been shown that thermo-diffusive pulsating instabilities can occur.[66, 45] The difficulty of obtaining gas flames with Lewis numbers much above unity means there has only been limited experimental observation of pulsating flames with this mechanism, although there is significant theoretical exploration of its existence.[58]

For travelling flames in tubes, a thermo-acoustic mechanism for pulsating instabilities can also complicate the characterization of pulsations.[27, 14, 53, 13] Unlike the thermo-diffusive instabilities that should only occur in lean mixtures, thermo-acoustic pulsating instabilities can form in both lean and rich mixtures. These thermo-acoustic instabilities are dependent on the dimension of the apparatus, being characterized by pulsations at harmonics of the fundamental frequency of the tube.[27, 14] These thermo-acoustic pulsations have been readily observed in gaseous and heterogeneous flames.

The fundamental frequency of the apparatus described in Section 2.2.2 can be calculated by simple consideration of the apparatus geometry. The fundamental frequency of a tube depends on its length and the speed of sound of the mixture in the tube, which is in turn dependent on the temperature of the mixture. For a tube with one open end and one closed end as in the present apparatus, the relation is simply

$$f_0 = \frac{v}{4L} = \frac{\sqrt{\gamma RT}}{4L} \tag{2.3}$$

where f_0 is the fundamental frequency, v is the speed of sound of the mixture in the tube, L is the length of the combustion tube plus the length of the diffuser cone and the ignition section, γ and R are the adiabatic index and gas constant, and T is the temperature. With a mixture of 60% oxygen and 40% argon at 300 K, the fundamental frequency of the shorter (0.6 m) tube is 100 Hz, and 50 Hz for the longer (1.4 m) tube. With a mixture of 15% oxygen and 85% argon and with 25% of the tube filled with combustion products at 3500 K (representing the

adiabatic flame temperature), the fundamental frequency increases to 200 Hz for the short tube, and 100 Hz for the longer tube.

All of the pulsations observed tend to be close to the fundamental frequency of the tube or a harmonic of the fundamental frequency. This can be seen in Figure 2–17b, where the bands on the right represent the fundamental frequencies and the harmonics for both the short and longer tube. There is some deviation in the frequencies observed compared to the fundamental frequency, however this could be explained due to changes in temperature affecting the sound speed of the mixture, and thus changing the fundamental frequency of the tube. Select tests in longer length tubes also show a reduction in the frequencies observed, in-line with the changing fundamental frequency of the tube. When the length of the tube was approximately doubled, the observed frequency of oscillation was observed to decrease by a factor of approximately two. This is apparent by comparing the lowest frequencies (corresponding to the fundamental frequency) for the trials in the short and long tubes in Figure 2–17b. This result is consistent with an oscillation that is coupled to the fundamental frequency of the tube. The frequencies of these pulsations are a good indication that thermo-acoustic instabilities determine the dominate frequency, however there is also evidence that the thermo-diffusive instability could be driving or influencing them. The pulsations are much more prominent in leaner mixtures where thermo-diffusive pulsations are predicted to occur, and the higher frequency pulsations are seen exclusively in leaner mixtures. Work by Clavin [14] on instabilities in two-phase flames in tubes has shown that the thermo-diffusive instability mechanism can

directly reinforce a thermo-acoustic pulsating instability. In Clavin's work, he comments that the complexity of this multi-dimensional instability makes it difficult to determine the specific mechanism behind the instability, however he showed that it is likely a combination of the thermo-diffusive and thermo-acoustic interactions that facilitate the formation of the instabilities. In addition, recent work by Julien et al. [31] has shown pulsations in the same aluminum fuel in unconfined, spherically propagating flames. As these flames are unconfined, there is no fundamental frequency associated with the environment in which they burn, and thus no mechanism for acoustical coupling of the flame front. This indicates that the pulsations observed in these spherically expanding flames are most likely to be thermo-diffusive in nature. Whether the oscillations observed in the tube experiments discussed in Section 2.2.6 are initiated by resonance with the tube acoustics or are a thermo-diffusive instability that becomes coupled to the tube fundamental frequency cannot be determined from the present experiments and would require further investigation.

2.3.2 Flame Speeds

The results of the experimental flame speed measurements reported in Figure 2–19 can be compared to the simple, theoretical models of continuum and discrete flame propagation discussed in Section 1.2. These models of flame propagation are highly idealized and not intended to model quantitative experimental results. Nonetheless, they can provide some assistance in interpreting experimental results.

The theoretical model uses the values for discreteness parameter seen in Table 2–3. The nondimensional ignition temperatures are calculated from the values in Table 2–4.

Table 2–4: Values used for calculating nondimensional ignition temperature of aluminum and iron mixtures.

		Aluminum	Iron
Unburned temperature	T_{u}	300 K	300 K
Ignition temperatrure	T_{ign}	2100 K	900 K
Adiabatic flame tempeature	T_{ad}	3570 K	2200 K
Nondimensional ignition temperature	θ_{ign}	0.55	0.32

In order to compare qualitative behaviour, the experimental flame speeds were averaged for each oxygen concentration, and normalized with respect to the theoretical results from the discrete model at 21% oxygen. The error bars represent a 95% confidence interval from the mean.

The iron results show the increase in flame speed with oxygen concentration follows the same trend as predicted by the continuous source term model. As the discreteness parameter is above unity, this model is sufficient to describe the behaviour of the flame, and the continuous and discrete models are in close agreement (as seen by the nearly identical prediction curves of the two models in Figure 2–20a). For the aluminum results (Figure 2–20b), the experimentally observed independence of flame speed on oxygen concentration correlates well with the behaviour predicted by the discrete source term model, while the continuous model predicts a continuously increasing flame speed with increasing oxygen concentration. The independence of flame speed on oxygen concentration is consistent with the theoretical predictions, as the discreteness parameter is below

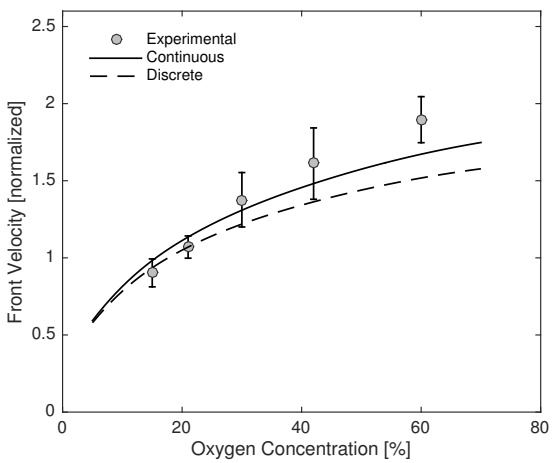

(a) Normalized iron flame speeds with comparison to continuous and discrete source term models.

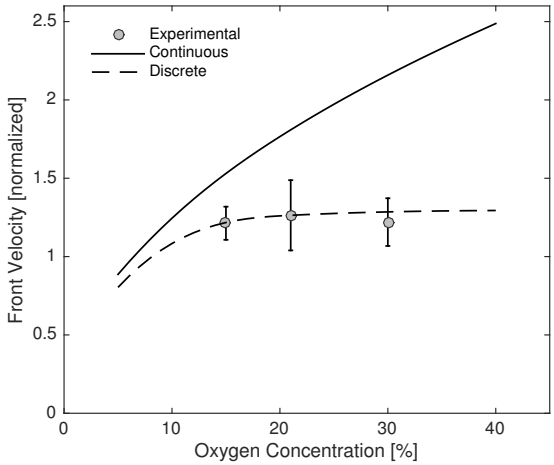

(b) Normalized aluminum flame speeds with comparison to continuous and discrete source term models.

Figure 2–20: Comparison of experimental results to model.

unity, necessitating a flame speed limited by heat diffusion rather than particle reaction time. At oxygen concentrations below 15%, the discrete source term model approaches the same behaviour as the continuous source term model. This convergence occurs because at lower oxygen concentrations, the particle reaction time is sufficiently short such that the discreteness parameter approaches unity.

2.4 Discussion

The attempts detailed above to experimentally verify the existence of the discrete regime highlight the significant challenges associated with realizing propagating laminar flames in particulate suspensions. The issues inherent to suspensions of particles under normal gravity conditions limit the particle size range and flame speeds, while the pulsating instabilities seen in lean mixtures limit the range of oxygen concentrations that can be tested. The use of smaller particles

(sub-micron) is not practical due to the inherent agglomeration of particles in this size range, making their uniform dispersion problematic and also making visualization of the individual particles difficult. Initial attempts at using large particle magnesium to facilitate direct visualization of the burning particles were described in Section 2.1, however this downwards-dispersing apparatus also encountered the added issue of convective recirculation cells that formed as the large particles quickly settle.[39] Although the intended independence of flame speed on oxygen concentration was observed, consistent with theoretical predictions from the discrete model, these issues made the mechanism behind this behaviour uncertain. The results from initial attempts using the Valimet H-5 aluminum powder as described in Section 2.2.5 also showed the same independence of flame speed on oxygen concentration, however the limited diagnostics prevented characterization of the pulsations observed, again making conclusions about the mechanism behind the behaviour problematic.

The range of flame speeds that can be observed is also limited. As discussed in Section 2.2.6, the larger oxygen concentrations that are required to observe faster flame propagation also promote intense instabilities (acoustic coupling, etc.) that would result in the flame quickly becoming turbulent. The use of lower oxygen concentration would, in principle, enable slower flames under lean conditions that would be ideal for studying the structure of the flame front, but under normal gravity conditions, the buoyancy-induced convection of the hot combustion products disrupts the flame, making flame propagation at velocities of less than 20 cm/s impractical to observe in the laboratory. Drop towers are limited

to test times of less than 10 seconds, and thus are not of sufficient duration to permit steady flame propagation to be observed, suggesting that the space-based reduced gravity environment (sounding rocket or on-orbit) will be required to observe ideal flame propagation in the discrete regime.

Despite these challenges, the current experiments enabled measurement of steady flame propagation in two different particulates (one iron, the other aluminum) in suspensions in gaseous oxidizer (oxygen/argon) over a select range of oxygen concentrations. While the range of oxygen concentration for the fast burning aluminum particulates was limited from 15 to 30% due to the flame instability issue described above, the measured flame speeds were seen to be insensitive to oxygen concentration over this range, in agreement with the discrete theory. The flame speeds for iron particulate suspensions exhibited a near square root dependence on oxygen concentration as it was varied from 15 to 60%, in agreement with classical flame theory.

The simple analytical model described in Section 1.2 and developed in detail in [62, 63] exhibits good qualitative agreement with the predicted trends in the experimental data. This agreement is in spite of the fact that the model neglects many physical processes present in real flame propagation, such as flow of the combustion products due to volumetric dilation of the gas, gas-particle slip, radiation, heat losses, thermophoresis, etc., in exchange for a physically intuitive formulation that makes the model amenable to an analytic solution. Despite these limitations, this simple analytical model is able to assist with interpretation of the

experimental results and, in particular, the independence of flame speed on oxygen concentration for aluminum fuel in a lean suspension.

In addition to the results presented in this paper, the recent experiments by Julien et al. [31] discussed in Section 2.3.1 examined flame propagation in unconfined clouds of aluminum in a gaseous oxidizer suspension under lean conditions and across a variety of inert balances, and reported similar results. Below stoichiometry, they noted an independence of flame speed with oxygen concentration, a result that cannot be explained by traditional continuous heterogeneous flame models. The spatial discreteness of the suspensions, wherein inter-particle heat diffusion, rather than the combustion rate, may be the restriction that limits flame propagation velocity under these conditions. The work by Julien et al. also observed cellular and pulsating instabilities similar to those that were observed in the present experiments, highlighting the thermo-diffusive nature of the instabilities.

CHAPTER 3
Microgravity Flame Propagation Experiments

3.1 Sounding Rocket Experiment

In order to overcome the significant challenges associated with performing dust combustion experiments, a sounding rocket platform is planned for launch in 2016 which will carry an apparatus designed to validate some predictions of the discrete flame propagation regime. This experiment will record the propagation of flames through suspensions of iron particles in different oxidizing environments. The Maxus-9 sounding rocket will launch to an apogee of over 700 km, which will provide 14 minutes of very high quality (10^{-4} g) microgravity.

In order to create a mixture which will operate in the discrete regime, the particle reaction time must be less than the inter-particle heat diffusion time. This can be achieved as in previous experiments by using a fuel which burns quickly, such as aluminum or magnesium, to reduce the particle reaction time. Alternatively, the inter-particle heat diffusion time can be increased, either by increasing the inter-particle spacing or by burning the fuel in a mixture with lower thermal diffusivity, such as with an oxygen/xenon mixture. This allows slower burning fuels such as iron to be used in place of aluminum or magnesium, and the discrete regime can still be accessed. Iron is preferable over aluminum or magnesium for a number of reasons. From a modelling perspective, the heterogeneous surface reactions inherent to the combustion of iron more

closely approximates the point like heat sources represented in the discrete source term model, avoiding the complex gas dynamic flow around the particle which would occur if gaseous intermediates or products were produced. In addition, the condensed phase oxides produced during iron combustion do not have the tendency to optically obscure the flame structure, nor coat the walls of the combustion apparatus with an oxide film. The vapour phase reactions of aluminum and magnesium means their oxides can cloud the structure of the flame, and in addition these oxides will coat the walls of the apparatus preventing multiple sequential trials in the same tube. Finally, it has been observed that iron flames are much less susceptible to the pulsating instabilities that have been observed in both aluminum and magnesium mixtures.

3.1.1 Experimental Apparatus

The sounding rocket hardware was designed by Airbus Defence and Space in collaboration with the European Space Agency, and is similar in principle to the lab-based flame propagation apparatus described in Section 2.2.2. Powder is dispersed into a transparent tube from one end, and ignition occurs at the opposite open end, propagating towards the closed dispersion end. The flight package will be 1.08 m long, 0.64 m in diameter, and weigh approximately 130 kg. The flight will feature both in-flight telemetry and telecommand.

Two different spherical iron powders, one with narrow particle size distributions of 20 to 25 μm and the other with 25 to 38 μm, will be used. A novel rotating brush dispersion system developed by Airbus Defence and Space will be used to create the suspension of iron particulates in gaseous suspension that will

be fed into the tubes. Based upon laboratory and parabolic flight experience, it is anticipated that a maximum of two experiments can be performed in each tube before the deposition of products on the tube wall affect the ability to observe the suspension and flame propagation. Thus, the tubes are mounted on a carousel system that rotates clean tubes into the field of view of the diagnostics. With 9 glass tubes per carousel and two carousels, a total of 36 combustion experiments can be planned, which would completely fill the available microgravity duration in the sounding rocket flight.

Flight experiments will begin with concentrations of 900 g/m^3 and then decrease in successive trials occurring during the flight to identify the propagation limit in different oxygen concentrations and diluent gases. Iron concentrations as low as 200 to 400 g/m^3 are possible. This will necessitate real-time control of the experiment from the ground station. The gaseous mixture used will be varied between 20% oxygen/80% xenon and 40% oxygen/60% xenon to investigate the flame propagation speed dependence upon oxygen concentration, and a control mixture of 20% oxygen/80% argon, which should result in a flame propagating in the continuum regime.

The diagnostic suite will consist of several cameras. Cameras intended to observe the flame structure will record at 60 fps and have a narrow field of view (33 cm^2) with a spatial resolution of 30 μm per pixel, sufficient to enable burning individual particles to be registered. Another camera focused upon a laser light sheet (520 nm green laser sheet with a height of 20 mm and a thickness

of 0.4 mm) will have a 32 cm^2 field of view and 23 μm per pixel to enable laser-illuminated particles to be observed. This camera will verify the uniformity of the particulate suspension and permit direct determination of particulate density with 5 fps sampling during the tube filling cycle. The flame speed camera will view the entire tube (304 cm^2 field of view) with 60 fps sampling and a spatial resolution of 150 μm per pixel. This camera must be located on the opposite side of the flight package from the tube it is observing, requiring an optical path that passes through the carousel. Finally, light emission data of the flame at various wavelengths will be recorded with a spectrometer with a resolution of 1.5 nm and a sampling rate of 20 spectra per second.

3.2 Parabolic Flight Campaign

3.2.1 Experimental Details

In order to support the technical and scientific development of the Maxus 9 suborbital sounding rocket experiment, a series of experiments on-board a parabolic flight research platform were performed. An on-going relationship between McGill University and the Canadian Space Agency has permitted the regular use of the Falcon-20 aircraft at the National Research Council in Ottawa. The most recent campaign was completed in February of 2014. The primary motivation of these series of experiments was to validate the test matrix that will be used on the Maxus 9 sounding rocket experiment.

The apparatus used was the same as that used for the laboratory based flame propagation experiments. The only changes were that the apparatus was rotated 90 degrees to rest on its side, as this allowed for better packaging and easier

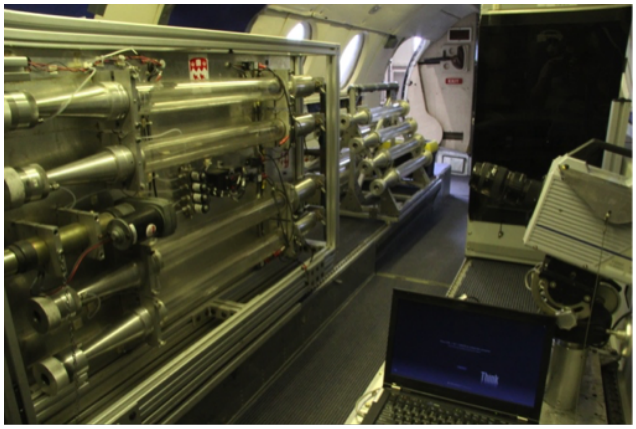

(a) Microgravity apparatus installed onboard Falcon-20 aircraft.

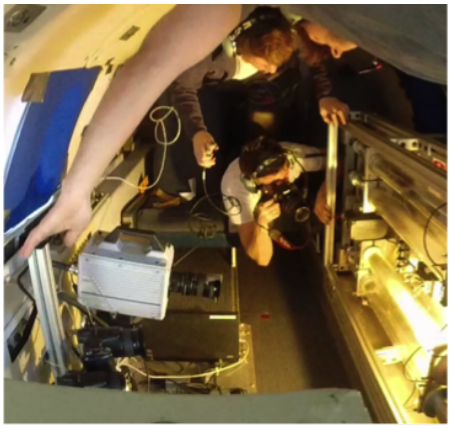

(b) Frame from GoPro camera showing overview of operation during parabola.

Figure 3–1: Apparatus and procedure for parabolic flight campaign.

operation on-board the aircraft, and the cyclone-based ventilation system was replaced with a vacuum system using replaceable multi-stage filters.

The diagnostic rack included a Photron SA-5 high-speed camera and two Casio EX-F1 high-speed cameras. The Photron SA-5 was operated at 2000 fps, and was focused on a region of the tube approximately 20 cm in length, to observe the structure of the flame. The Casio cameras were operated at 300 fps and 30 fps, and recorded the full length of the tube in order to obtain flame speed measurements and a real-time view of flame propagation. A GoPro camera was also mounted in the cabin of the aircraft to provide a high-level overview of the cabin operating procedures.

A total of 8 flights were performed over a week, with 12 parabolas during each flight. The tests included trials with both iron and magnesium powders of various particle sizes dispersed in four different oxidizing mixtures. For iron, the

size distributions used were sub 25 μm, 25-38 μm, and 45-53 μm. For magnesium, the sizes tested were 25-38 μm, 45-53 μm, and 53-75 μm. The ternary inert-nitrogen-oxygen gas mixtures used in this campaign allowed the specific heat of the gas mixture to remain constant while changing oxygen concentration. The gas mixtures were factory premixed with accuracy better than $\pm 0.5\%$ and contained 15, 20, 40, and 60% oxygen, each with 40% argon and a nitrogen balance.

3.2.2 Results

Test Matrix

The major purpose of defining boundaries of the test matrix was to identify an envelope of particle sizes and oxygen concentration within which flame propagation is possible. The test matrix results provided valuable experimental points for identifying the flame propagation boundaries in the 10^{-2} g environment characteristic for parabolic flight. These results are shown in Tables 3–1 and 3–2.

Table 3–1: Test matrix for iron powders.

O_2%	-25 μm		25–38 μm		38–45 μm		45–53 μm	
	Go	No-go	Go	No-go	Go	No-go	Go	No-go
15		4						
20	6			12				6
40	10		15	3				4
60	3	1	10	2		4		

The results showed that flame propagation was much less consistent at larger particle sizes and lower oxygen concentrations. This helps define the test matrix for the Maxus 9 sounding rocket experiment.

Table 3–2: Test matrix for magnesium powders.

O_2%	25–38 μm		38–45 μm		45–53 μm		53–75 μm	
	Go	No-go	Go	No-go	Go	No-go	Go	No-go
15	4				2	2		
20								
40					2	1		
60							1	3

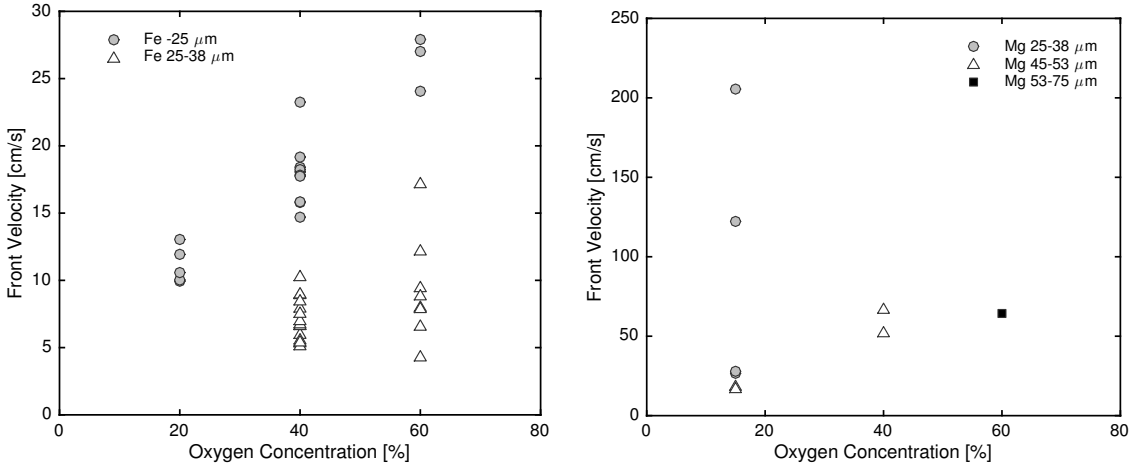

(a) Flame speeds of iron at different oxygen concentrations in microgravity environment.

(b) Flame speeds of magnesium at different oxygen concentrations in microgravity environment.

Figure 3–2: Measured flame speeds in parabolic microgravity flight campaign

Flame Speeds

In addition to determining the propagation envelope, measurements of the flame speeds observed were also intended to provide further validation for the continuous and discrete regimes. The slow burning iron powders are mixtures which burn in the continuous regime, while the magnesium powders burn quickly and will operate in the discrete regime, as described in Sections 2.1.4 and 2.2.4.

The results obtained for iron confirm the flame behaviour consistent with the continuous regime of flame propagation, including a dependence of flame speeds on oxygen concentration and particle size. The lack of data points available for magnesium prevents the formation of a definitive conclusion for whether it is indeed evidence of the discrete regime, but provides motivation for continued tests.

3.3 Discussion

The unique microgravity environment enables reactive wave propagation to be observed under conditions that cannot be realized under the normal gravity environment. The ability to create uniform, quiescent suspensions of particulates permits a well-characterized medium with highly discrete sources of heat to be realized. The absence of buoyancy-driven convection means that extremely slow ($\sim$1 cm/s) reactive waves in discrete media can be observed wherein the propagation is determined by the inter-particle diffusion time, rather than the energy release rate and global thermal gradient, as in the case in traditional flames. The parabolic flight experiments helped define the test matrix for the Maxus 9 sounding rocket experiment, which hopes to validate the discrete theory under conditions not achievable using conventional experimental techniques.

CHAPTER 4
Single Particle Experiments

4.1 Motivation

The single particle burning time of iron is a key parameter for determining the discreteness parameter for the iron mixtures that will be used on the Maxus 9 sounding rocket experiment. This data is not available in the literature, which necessitates experimental measurement for verification. The burn time of a particle is a fundamental property used in many combustion models, which provides additional relevance for such experiments.[18] The experimental techniques developed can also be extended to the measurement of single particle burn times of other materials.

4.2 Experimental Apparatus

The apparatus consists of two high temperature tube furnaces connected inline with a ceramic tube running the full length of both furnaces. The gas inlet is situated at the entrance to the first furnace and creates an adjustable flow of gas through the ceramic tube. The gas inlet allows for control of the oxidizing environment. The outlet of the second furnace is connected to a transparent fused silica tube with a metal connecting sleeve. A semi-circular heater covers one half of the silica tube to maintain a high temperature. The particle dispersion system allows single particles to be injected into the sleeve connector, where the hot gas flowing at around 4 m/s pushes the particles into the silica tube where they ignite.

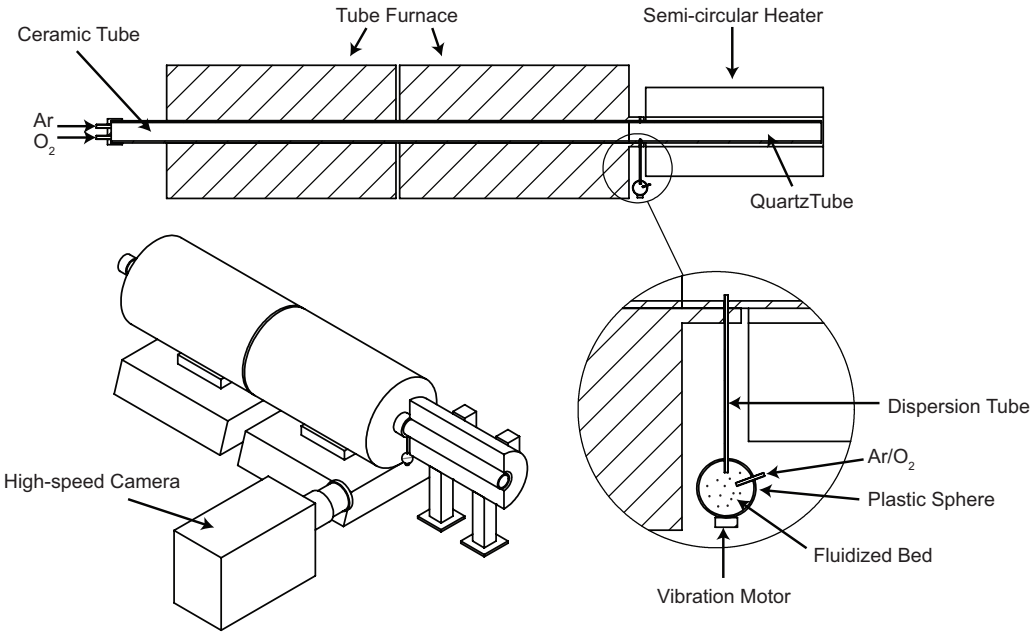

Figure 4–1: Top: Cross sectional view of single particle ignition experiment. Bottom: Isometric view of full apparatus and detailed view of dispersion system.

The injection is achieved by pressurizing a fluidized bed in a vibrating plastic sphere to force single particles through a thin tube into the connecting sleeve. K-type thermocouples measure the temperature at the particle inlet and along the silica tube. The temperature is maintained at around 1000 K throughout the silica tube.

In order to measure the burning times of the particles, a Photron Fastcam SA-5 high-speed camera operating between 2000 and 4000 fps visually captures the ignition events. A DSLR camera is also used for long exposure photographs of the single particle streaks.

4.3 Microscope Sizing Technique

The iron particles being tested are sieved through a series of standard sieves in order to obtain narrow particle size distributions. A fast and accurate automated particle sizing technique using off the shelf components was developed in order to obtain the exact size distributions of these cohorts. This allows for the correlation of burning time and ignition temperature with particle size. Using a digital camera attached to a standard optical microscope, a series of images are taken of particles distributed on a microscope slide. A MATLAB script automatically parses a statistically significant number of these images, and measures the diameter of each visible and non-agglomerated particle. The sizing method works best for relatively spherical particles. Hundreds of particles are analyzed for each cohort, and fitting one term Gaussian functions to each gives adjusted R^2 values of over 98%. The process and typical results are shown in Figure 4–2.

4.4 Fuel and Oxidizer

The burning times of two iron powders were tested. The first was a spherical powder manufactured by Sandvik Osprey Powders. The second powder was a spheroidal powder manufactured by Alfa Aesar. Images and the size distributions of these powders are shown in Figures 4–3 and 4–4. The two powders have different levels of impurities. These are compared in Table 4–1. The Sandvik Osprey Powder has large traces of carbon, silicon, and manganese. The amounts of these elements makes the powder close in composition to a high carbon steel,

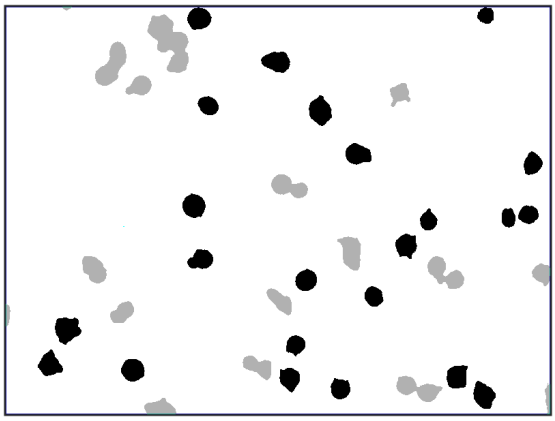

(a) Particle sizing processing for single image. Black denotes measured particles, gray is ignored particles (agglomerated or touching sides).

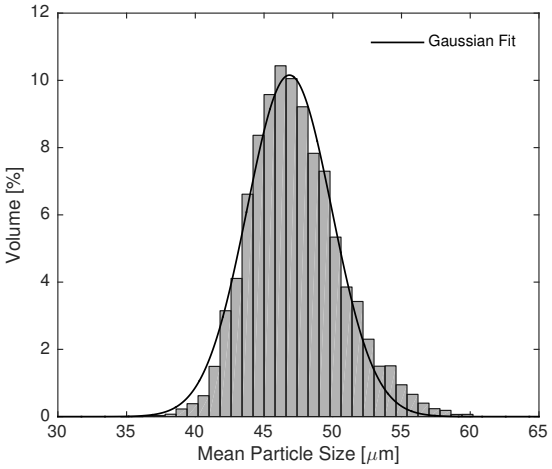

(b) Histogram and gaussian fit obtained with microscope sizing technique. Adjusted R^2 value of 98.4%.

Figure 4–2: Microscope particle sizing technique.

rather than iron. The Alfa Aesar powder is very close to pure iron, with only negligible amounts of trace elements.

Table 4–1: Composition of iron powders tested in single particle apparatus.

	Sandvik Osprey	Alfa Aesar
Iron	98.37%	99.9%
Carbon	0.40%	0.006%
Manganese	0.61%	0.001%
Silicon	0.62%	0.002%
Sulfer	-	0.002%
Nickel	-	0.01%
Phosphorus	-	0.001%

The burning times were measured in three different oxidizing environments, each with argon as an inert. They included 21%, 42%, and 60% oxygen, with

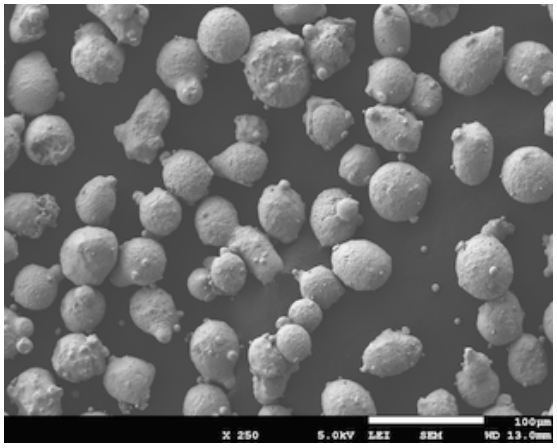

(a) SEM photo of Sandvik Osprey iron, 38–45 μm.

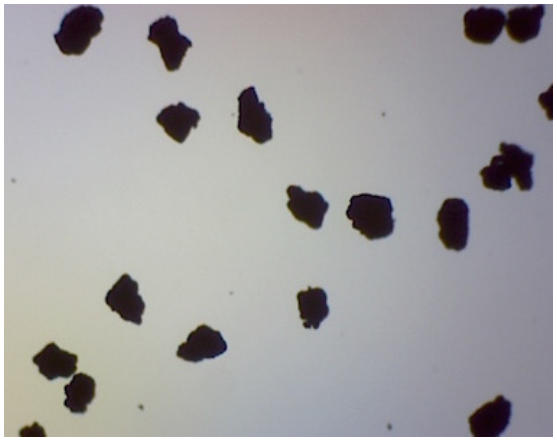

(b) Optical microscope image of Alfa Aesar iron, 53–63 μm.

Figure 4–3: Visual details of iron powders tested.

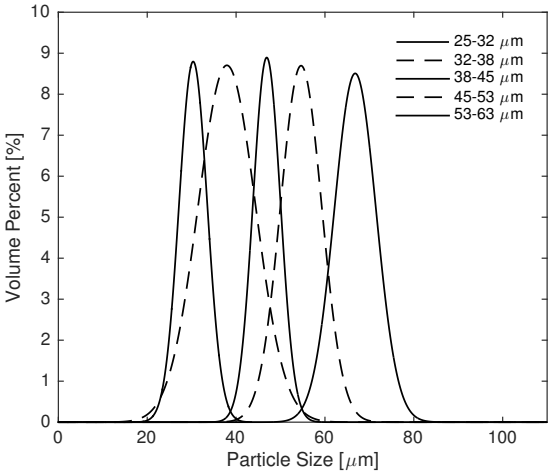

(a) Sieved size distributions for Sandvik Osprey iron powder with impurities.

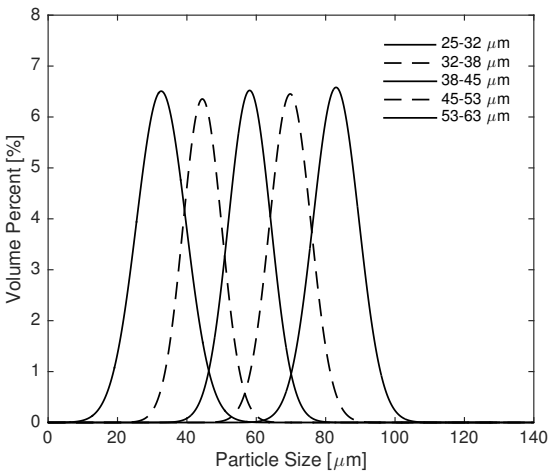

(b) Sieved size distributions for Alfa Aesar pure iron powder.

Figure 4–4: Size distributions of tested powders.

argon as the balance. The gases were commercially supplied and certified by Praxair to an accuracy of ±0.8%, and verified with an oxygen analyser.

For the range of parameters being tested in this study, the burning rate is expected to be predominantly diffusion-limited [60].

4.5 Results

4.5.1 Iron with Impurities

Early trials revealed that the burning of the Sandvik Osprey iron particles with impurities terminate with a micro-explosion of the particles, rather than a gradual burnout. The particles break up into smaller pieces which quickly burnout. This can be seen clearly in Figure 4–5. This is similar to the behaviour of burning titanium particles [43, 1]. For titanium particles, the mechanism behind the explosion is thought to be due to dissolved gases in the particles expanding as they are heated, until they violently force the particle apart. Attempts at degassing the iron particles under high temperature vacuum conditions did not affect the behaviour of the particle combustion. This behaviour meant that instead of a time to burnout, a time to explosion was measured instead. This is the same methodology used for measuring the burning properties of single titanium particles.[10]

The high-speed videos captured of these particles burning were processed automatically using a MATLAB script. This script tracks each particle, and records the time from ignition to explosion for each particle. The results are verified manually. These results are shown in Figure 4–6. The x-values represent the average of each size distribution, with the error bars representing one standard

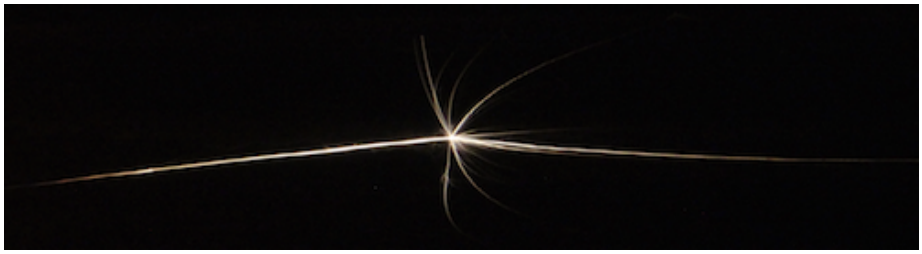

Figure 4–5: Long exposure photograph from DSLR of iron particle with impurities terminating with explosion during burning process.

deviation of the size distribution. The y-values represent the average time to explosion for measurements of between 15 and 100 particles, with the error bars again representing one standard deviation in time to explosion.

4.5.2 Pure Iron

The burning behaviour of the pure Alfa Aesar iron showed that these particles burn with the expected gradual burnout, rather than terminating with an explosion. After ignition, the brightness of the particles increases until it reaches a maximum, and then gradually decreases as the particle burns out. It was also observed that after the light intensity has decreased to a minimum, the majority of times it would then briefly increase slightly before finally burning out completely. These behaviours are shown in Figure 4–7.

The high-speed video of the burning of these particles were processed in a similar manner to the Sandvik Osprey iron. A MATLAB script automatically tracked each particle, and recorded the time from ignition to complete burnout. The results are shown in Figure 4–8. The x-values represent the average of each size distribution, with the error bars representing one standard deviation of the size distribution. The y-values represent the average time to burnout

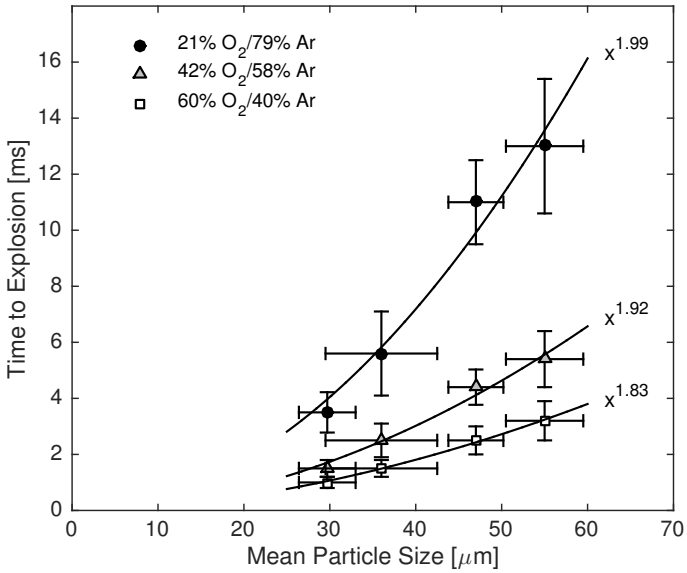

Figure 4–6: Results for time to explosion of iron with impurities.

Figure 4–7: Long exposure photograph from DSLR of pure iron particle gradually burning out.

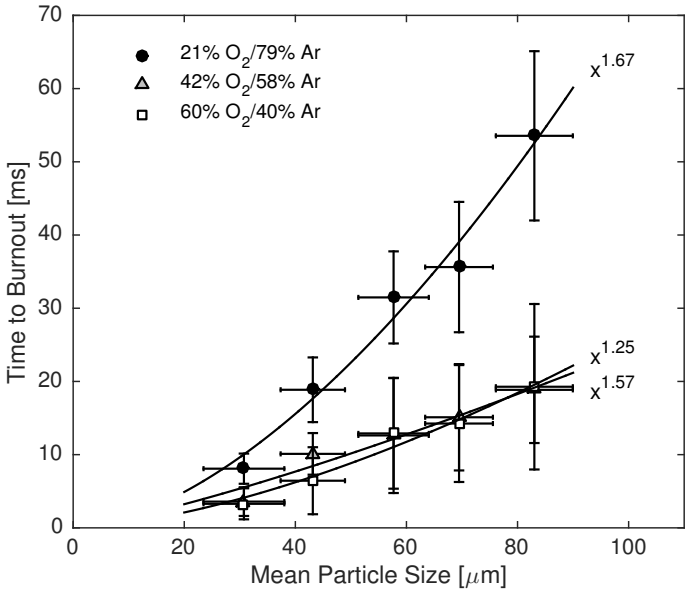

Figure 4–8: Results for time to burnout of pure iron.

for measurements of between 15 and 100 particles, with the error bars again representing one standard deviation in burnout time.

In an attempt to compare the results to the time to explosion of the Sandvik Osprey powder, the processing script also recorded the time from ignition to maximum brightness of the particle. The results of this are shown in Figure 4–9.

4.6 Analysis and Discussion

Due to the relatively large sizes of the particles tested, and the relatively low diffusivity argon inert used in the oxidizer, the burning rate for our particles is expected to be diffusion-limited [60]. Figure 4–10 shows the expected relationship between burning time and particle diameter for particles that burn in the diffusion-limited mode, as calculated from Equation 1.8. The values used for these calculations are shown in Table 4–2. The values are obtained assuming a balance

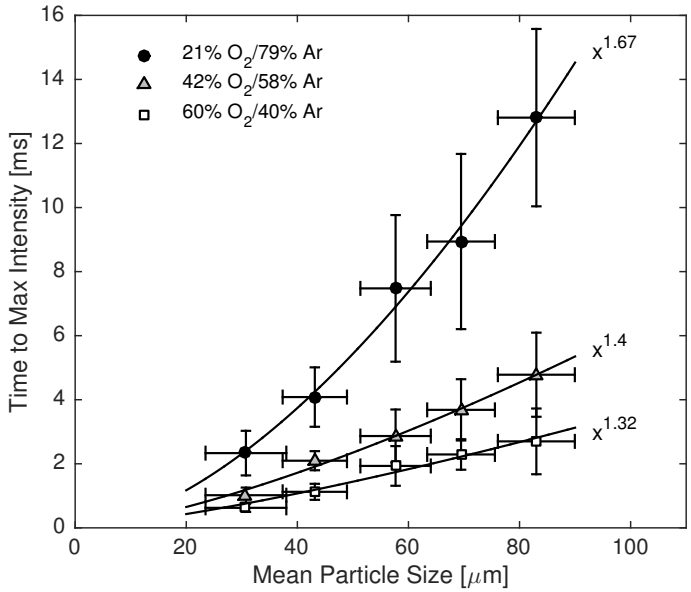

Figure 4–9: Results for time to maximum brightness of iron with impurities.

of argon, the temperature of the oxidizing environment is taken at 1000 K, the mass diffusivity is calculated from the Chapman-Enskog theory, and the mass stoichiometric index is calculated assuming Fe_2O_3 as the oxide.

Table 4–2: Values used for calculating single particle iron burn times.

		Oxygen Concentration		
		21%	42%	60%
Particle density	ρ	7650 kg/m^3	7650 kg/m^3	7650 kg/m^3
Gas density	ρ_s	0.47 kg/m^3	0.45 kg/m^3	0.43 kg/m^3
Mass diffusivity of oxygen	D	$1.6{\cdot}10^{-4}$ m^2/s	$1.6{\cdot}10^{-4}$ m^2/s	$1.6{\cdot}10^{-4}$ m^2/s
Mass stoichiometric index	i	2.33	2.33	2.33
Mass fraction of oxygen	$m_{0\infty}$	0.18	0.47	0.55

For the Sandvik Osprey powder with impurities, the explosion behaviour of the particles makes the influence of the d^2 law uncertain. Quantitatively, the times to explosion are an order of magnitude lower compared to what is predicted

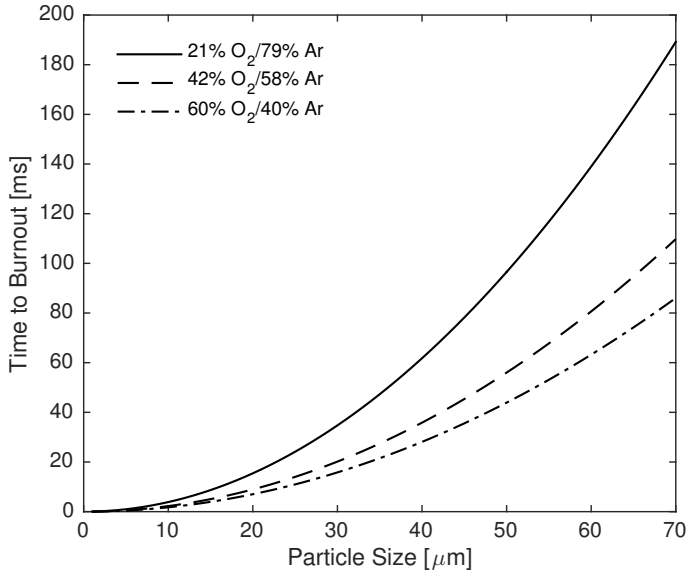

Figure 4–10: Theoretical burning times for iron in different oxygen concentrations, demonstrating the d^2 law.

with the d^2 law. This can be explained because it is likely that only a fraction of the iron has been consumed before the particle explodes. The results, however, show very close qualitative agreement with the predicted behaviour. The time to explosion increases with increasing particle size, and fitting a power law to the results shows exponent values between 1.83 and 1.99, close to the value of 2 predicted with the d^2 law. The burning time also appears to decrease with oxygen concentration in similar proportions to what was predicted. This may indicate that the onset of explosion occurs consistently at the same point in the burning process.

The results for the pure Alfa Aesar iron powder show slightly different results. The quantitative behaviour is closer to that predicted by the d^2 law, however it is still lower by a factor of around 3. The d^2 law is a conceptually simple model which neglects many factors, and so exact agreement is not expected.

Qualitatively, there is also some disagreement between the experimental results and the predicted trends. The power law fits show exponents ranging from 1.25 to 1.67, much less than the predicted 2, and the results for the 42% and 60% oxidizer are very similar in value. The reduced exponent may indicate a transition to a partially kinetically controlled regime.

The results showing time to maximum intensity, rather than time to burnout, show slightly better qualitative agreement. The exponents are still lower than predicted, ranging from 1.32 to 1.67, however now there is a clear separation between the 42% and 60% cases. The quantitative results for this graph are also now of the same order as the results seen for time to explosion of the Sandvik Osprey iron with impurities. This may indicate the explosion behaviour for the iron with impurities occurs shortly after attaining maximum brightness.

Similar unsteady combustion behaviour of single particles has been seen for titanium, as mentioned previously, and also aluminum, where unsteady spinning or oscillatory behaviour can be seen.[6, 52] The exact mechanisms for these behaviours is still not known; however, some of the explanations proposed include superheating of the droplet, interaction of oxygen-nitrogen compounds with the metal on the particle surface, compositional variations, or temperature variations.[52] Although the physical mechanism behind these explosions is not known, the empirical behaviour of the sparks produced by different metals has been known for over a century. Machinists have used a technique known as "spark testing" for determining the composition of unknown metals. Solid pieces of the metal are held on a grinding wheel, and the visual appearance of the sparks can

be used to determine the composition of the metal. Figure 4–11 shows images from a machinery handbook published in 1918 describing the sparking behaviour of different metals. It can be seen that the carbon and manganese content can influence the sparks to terminate with an explosion, much like the behaviour seen in this experimental investigation.

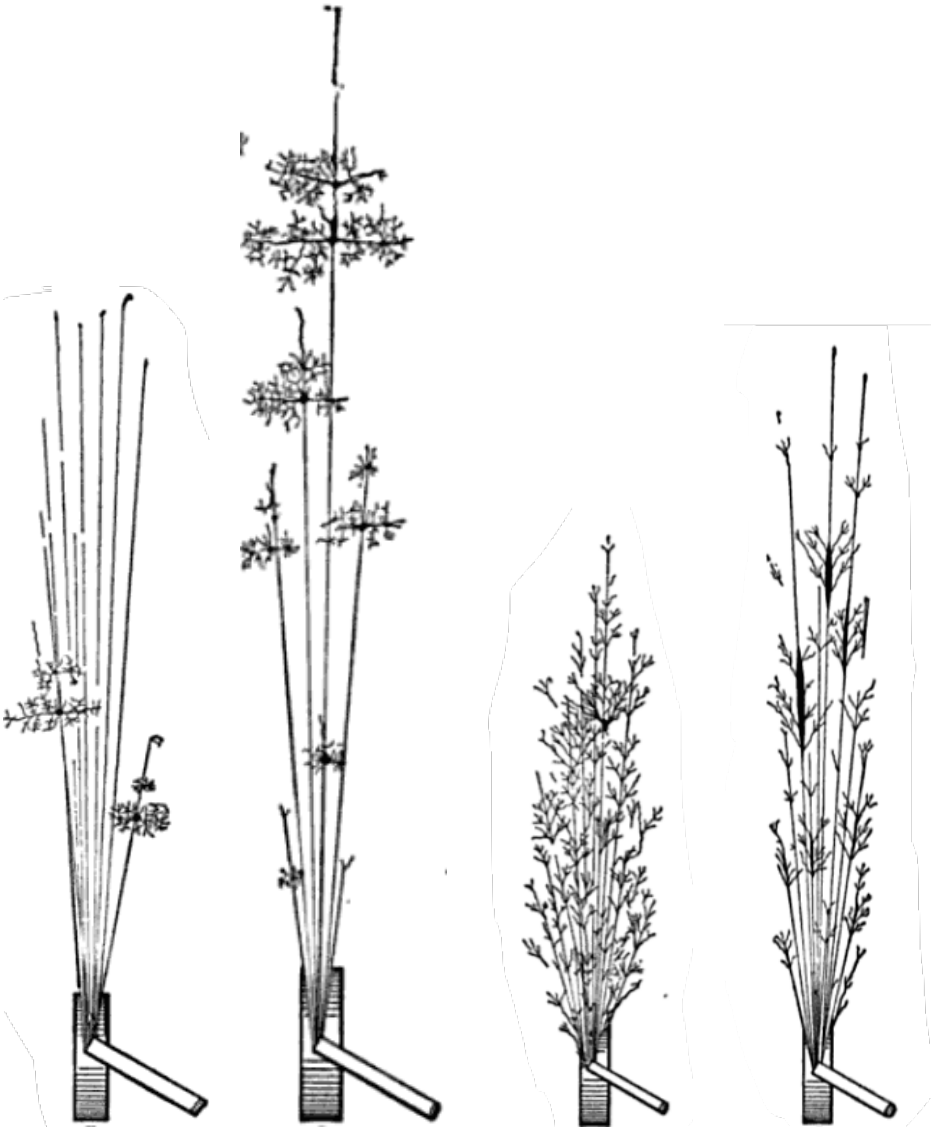

(a) Mild steel. C<0.3%.

(b) Steel. 0.5%<C<0.85%.

(c) High-carbon steel. 0.55%<C<0.95%, 0.3%<Mn<0.9%.

(d) Manganese steel. Mn∼13%.

Figure 4–11: Sparking behaviour of different metals. Images taken from [46].

CHAPTER 5
Conclusions

The discrete regime of flame propagation in heterogeneous media necessitates that the spatial discreteness of the localized particles be taken into account in modelling the flame front. The effects of discreteness lead to some unique behaviour, including a lack of dependence of flame speed on particle combustion time for sufficiently short combustion times (i.e., short in comparison to the inter-particle diffusion time). The flame speed becomes limited by the inter-particle heat diffusion, rather than the particle reaction rate. This behaviour was experimentally validated with an apparatus that allows for the measurement of flame speeds for lean suspensions of faster burning aluminum in oxygen/argon mixtures with varying oxygen concentration. As the oxygen concentration was increased, effectively reducing the particle reaction time by a proportional amount, the flame speed was seen to be invariant. A control case of slower burning iron particles that have large (greater than unity) non-dimensional combustion times exhibited the expected increase in flame speed, varying approximately with the square root of the oxygen concentration. The significant challenges inherent to dust combustion experiments motivate the need for further testing in the microgravity environment, particularly in the longer duration, high quality microgravity provided by sounding rocket and orbital-based platforms. The burning times of single particle iron powders were measured to validate parameters for the sounding rocket experiment

planned for launch in 2016. The results showed that the purity of the iron can dramatically influence the burning mechanism. The qualitative behaviour was consistent with a predominantly diffusively-controlled burning mode, however at high oxygen concentrations there is evidence of a transition to a partially kinetically controlled burning rate.

References

[1] C. Badiola and E. Dreizin. Combustion of micron-sized particles of titanium and zirconium. *Proceedings of the Combustion Institute*, 34(2):2237–2243, 2013.

[2] D. Ballal. Flame Propagation Through Dust Clouds of Carbon, Coal, Aluminium and Magnesium in an Environment of Zero Gravity. *Proceedings of the Royal Society A: Mathematical, Physical and Engineering Sciences*, 385(1788):21–51, 1983.

[3] D. Beach, A. Rondinone, B. Sumpter, S. Labinov, and R. Richards. Solid-State Combustion of Metallic Nanoparticles: New Possibilities for an Alternative Energy Carrier. *Journal of Energy Resources Technology*, 129(1):29, 2007.

[4] J. Beck and V. Volpert. A simple model of two-dimensional solid flame microstructure. *Combustion Theory and Modelling*, 7(4):795–812, 2003.

[5] J. Beck and V. Volpert. Nonlinear dynamics in a simple model of solid flame microstructure. *Physica D: Nonlinear Phenomena*, 182(1-2):86–102, 2003.

[6] M. Beckstead. A Summary of Aluminum Combustion. Technical report, Brigham Young University, 2004.

[7] M. Beckstead. Correlating Aluminum Burning Times. *Combustion, Explosion and Shock Waves*, 41(5):533–546, 2005.

[8] J. Bergthorson, S. Goroshin, M. Soo, P. Julien, J. Palecka, D. Frost, and D. Jarvis. Direct combustion of recyclable metal fuels for zero-carbon heat and power. *Applied Energy*, 160:368–382, 2015.

[9] V. Boiko, V. Lotov, and A. Papyrin. Ignition of gas suspensions of metallic powders in reflected shock waves. *Combustion, Explosion and Shock Waves*, 25(2):193–199, 1989.

[10] M. Cairns, D. Frost, and S. Goroshin. Effect of Oxygen Concentration on the Combustion of Titanium Particles. *International Colloquium on the Dynamics of Explosions and Reactive Systems*, pages 25–28, 2009.

[11] H. Cassel and I. Liebman. Combustion of magnesium particles I. *Combustion and Flame*, 6(0):153–156, 1962.

[12] H. Cassel and I. Liebman. Combustion of magnesium particles II, Ignition temperatures and thermal conductivities of ambient atmospheres. *Combustion and Flame*, 7(0):79–81, 1963.

[13] C. Clanet, G. Searby, and P. Clavin. Primary acoustic instability of flames propagating in tubes: cases of spray and premixed gas combustion. *Journal of Fluid Mechanics*, 385:157–197, 1999.

[14] P. Clavin and J. Sun. Theory of Acoustic Instabilities of Planar Flames Propagating in Sprays or Particle-Laden Gases. *Combustion Science and Technology*, 78(4-6):265–288, 1991.

[15] S. Dawson, J. Keizer, and J. Pearson. Fire-diffuse-fire model of dynamics of intracellular calcium waves. *Proceedings of the National Academy of Sciences*, 96(11):6060–6063, 1999.

[16] E. Dreizin. Experimental study of aluminum particle flame evolution in normal and micro-gravity. *Combustion and Flame*, 116(3):323–333, 1999.

[17] R. Eckhoff. *Dust explosions in the process industries: identification, assessment and control of dust hazards*. Gulf Professional Publishing, Houston, 2003.

[18] I. Glassman and R. Yetter. Combustion of Nonvolatile Fuels. In *Combustion*, pages 495–548. Academic Press, 4th edition, 2008.

[19] S. Goroshin, M. Bidabadi, and J. Lee. Quenching distance of laminar flame in aluminum dust clouds. *Combustion and Flame*, 105(12):147–160, 1996.

[20] S. Goroshin, I. Fomenko, and J. Lee. Burning velocities in fuel-rich aluminum dust clouds. *Symposium (International) on Combustion*, 26(2):1961–1967, 1996.

[21] S. Goroshin, A. Higgins, L. Jiang, K. MacKay, and P. Ashrit. Gasless combustion-driven heating elements for materials experiments in space. *Microgravity - Science and Technology*, 16(1-4):322–327, 2005.

[22] S. Goroshin, A. Higgins, and M. Kamel. Powdered metals as fuel for hypersonic ramjets. *AIAA Paper 2001-3919*, 2001.

[23] S. Goroshin, A. Higgins, and J. Lee. Powdered magnesium-carbon dioxide propulsion concepts for Mars missions. *AIAA Paper 1999-2408*, 1999.

[24] S. Goroshin, M. Kolbe, J. Bellerose, and J. Lee. Microgravity Apparatus and Ground-Based Study of the Flame Propagation and Quenching in Metal Dust Suspensions. In *Seventh International Workshop on Microgravity Combustion and Chemically Reacting Systems*, page 341, 2003.

[25] S. Goroshin, J. Lee, and Y. Shoshin. Effect of the discrete nature of heat sources on flame propagation in particulate suspensions. *Symposium (International) on Combustion*, 27(1):743–749, 1998.

[26] S. Goroshin, J. Mamen, A. Higgins, T. Bazyn, N. Glumac, and H. Krier. Emission spectroscopy of flame fronts in aluminum suspensions. *Proceedings of the Combustion Institute*, 31:2011–2019, 2007.

[27] S. Goroshin, V. Shevchuk, and N. Ageev. Oscillatory combustion of gaseous suspensions. *Combustion, Explosion, and Shock Waves*, 17(6):595–600, 1981.

[28] S. Goroshin, F. Tang, and A. Higgins. Reaction-diffusion fronts in media with spatially discrete sources. *Physical Review E*, 84(2):27301, 2011.

[29] S. Goroshin, F. Tang, A. Higgins, and J. Lee. Laminar dust flames in a reduced-gravity environment. *Acta Astronautica*, 68(78):656–666, 2011.

[30] A. Hepp, D. Linne, G. Landis, M. Wade, and J. Colvi. Production and Use of Metals and Oxygen for Lunar Propulsion. *Journal of Propulsion and Power*, 10(6):834–840, 1994.

[31] P. Julien, J. Vickery, S. Goroshin, D. Frost, and J. Bergthorson. Freely-propagating flames in aluminum dust clouds. *Combustion and Flame*, 2015.

[32] J. Keizer, G. Smith, S. Ponce-Dawson, and J. Pearson. Saltatory propagation of Ca2+ waves by Ca2+ sparks. *Biophysical Journal*, 75(2):595–600, 1998.

[33] C. Law. Aerodynamics of Laminar Flames. In *Combustion Physics*, pages 396–471. Cambridge University Press, 2006.

[34] C. Law and F. Williams. Combustion of magnesium particles in oxygen-inert atmospheres. *Combustion and Flame*, 22(3):383–405, 1974.

[35] B. Legrand, M. Marion, C. Chauveau, I. Gokalp, and E. Shafirovich. Ignition and Combustion of Levitated Magnesium and Aluminum Particles in Carbon Dioxide. *Combustion Science and Technology*, 165(1):151–174, 2001.

[36] B. Legrand, E. Shafirovich, M. Marion, C. Chauveau, and I. Gökalp. Ignition and combustion of levitated magnesium particles in carbon dioxide. *Symposium (International) on Combustion*, 27(2):2413–2419, 1998.

[37] I. Liebman, J. Corry, and H. Perlee. Ignition and Incendivity of Laser Irradiated Single Micron-Size Magnesium Particles. *Combustion Science and Technology*, 5(1):21–30, 1972.

[38] M. Marion, C. Chauveau, and I. Gökalp. Studies on the Ignition and Burning of Levitated Aluminum Particles. *Combustion Science and Technology*, 115(4-6):369–390, 1996.

[39] W. Mason and K. Saunders. Recirculating flow in vertical columns of gas-solid suspension. *Journal of Physics D: Applied Physics*, 8(14):1674, 1975.

[40] A. Merzhanov. The chemistry of self-propagating high-temperature synthesis. *Journal of Materials Chemistry*, 14(12):1779–1786, 2004.

[41] X. Mi, S. Goroshin, A. Higgins, R. Stowe, and S. Ringuette. Dual-stage ignition of boron particle agglomerates. *Combustion and Flame*, 160(11):2608–2618, 2013.

[42] I. Mitkov. One-and two-dimensional wave fronts in diffusive systems with discrete sets of nonlinear sources. *Physica D: Nonlinear Phenomena*, 133(1-4):398–403, 1999.

[43] I. Molodetsky, E. Vicenzi, E. Dreizin, and C. Law. Phases of titanium combustion in air. *Combustion and Flame*, 112:522–532, 1998.

[44] A. Mukasyan and A. Rogachev. Discrete reaction waves: Gasless combustion of solid powder mixtures. *Progress in Energy and Combustion Science*, 34(3):377–416, 2008.

[45] C. Nicoli, P. Haldenwang, and S. Suard. Analysis of pulsating spray flames propagating in lean two-phase mixtures with unity Lewis number. *Combustion and Flame*, 143(C):299–312, 2005.

[46] E. Oberg and F. Jones. *Iron and steel; a treatise on the smelting, refining, and mechanical processes of the iron and steel industry*. Industrial Press, 1918.

[47] H. Pearlman and P. Ronney. Near-limit behavior of high-Lewis number premixed flames in tubes at normal and low gravity. *Physics of Fluids*, 6(12):4009, 1994.

[48] N. Peters. Laminar diffusion flamelet models in non-premixed turbulent combustion. *Progress in Energy and Combustion Science*, 10(3):319–339, 1984.

[49] V. Prachukho, E. Ozerov, and A. Yurinov. Burning of magnesium particles in water vapor. *Combustion, Explosion and Shock Waves*, 7(2):195–198, 1971.

[50] T. Roberts, R. Burton, and H. Krier. Ignition and combustion of aluminum-magnesium alloy particles in O_2 at high pressures. *Combustion and Flame*, 92(12):125–143, 1993.

[51] A. Rogachev and A. Mukasyan. Experimental verification of discrete models for combustion of microheterogeneous compositions forming condensed combustion products (Review). *Combustion, Explosion, and Shock Waves*, 51(1):53–62, 2015.

[52] P. Ronney. Premixed-gas Flames. In H. Ross, editor, *Microgravity Combustion: Fire in Free Fall*, pages 35–82. Academic Press, 2001.

[53] G. Searby. Acoustic Instability in Premixed Flames. *Combustion Science and Technology*, 81:221–231, 1992.

[54] E. Shafirovich and U. Goldshleger. Combustion of Magnesium Particles in CO_2/CO Mixtures. *Combustion Science and Technology*, 84(1-6):33–43, 1992.

[55] E. Shafirovich and U. Goldshleger. The superheat phenomenon in the combustion of magnesium particles. *Combustion and Flame*, 88(34):425–432, 1992.

[56] E. Shafirovich and A. Varma. Metal-CO_2 Propulsion for Mars Missions: Current Status and Opportunities. *Journal of Propulsion and Power*, 24(3):385–394, 2008.

[57] V. Shevtsov, V. Fursov, and L. Stesik. Mechanism for combustion of isolated magnesium particles. *Combustion, Explosion and Shock Waves*, 12(6):758–763, 1976.

[58] K. Shkadinskii, B. Khaikin, and A. Merzhanov. Propagation of a pulsating exothermic reaction front in the condensed phase. *Combustion, Explosion, and Shock Waves*, 7(1):15–22, 1971.

[59] J. Sun, R. Dobashi, and T. Hirano. Combustion Behavior of Iron Particles Suspended in Air. *Combustion Science and Technology*, 150(February 2015):99–114, 2000.

[60] F. Tang, S. Goroshin, and A. Higgins. Modes of particle combustion in iron dust flames. *Proceedings of the Combustion Institute*, 33(2):1975–1982, 2011.

[61] F. Tang, S. Goroshin, A. Higgins, and J. Lee. Flame propagation and quenching in iron dust clouds. *Proceedings of the Combustion Institute*, 32(2):1905–1912, 2009.

[62] F. Tang, A. Higgins, and S. Goroshin. Effect of discreteness on heterogeneous flames: Propagation limits in regular and random particle arrays. *Combustion Theory and Modelling*, 13(2):319–341, 2009.

[63] F. Tang, A. Higgins, and S. Goroshin. Propagation limits and velocity of reaction-diffusion fronts in a system of discrete random sources. *Physical Review E*, 85:1–10, 2012.

[64] A. Valov, E. Gusachenko, and V. Shevtsov. The effect of CO_2 pressure and concentration on the ignition of single Mg particles in C-Ar mixtures. *Combustion, Explosion and Shock Waves*, 28(1):7–10, 1992.

[65] A. Valov, Y. Kustov, and V. Shevtsov. Spectroscopic study of the combustion of solitary magnesium particles in air and in carbon dioxide. *Combustion, Explosion and Shock Waves*, 30(4):431–436, 1994.

[66] R. Weber, G. Mercer, H. Sidhu, and B. Gray. Combustion waves for gases (Le = 1) and solids (Le $\rightarrow \infty$). *Proceedings of the Royal Society A: Mathematical, Physical and Engineering Sciences*, 453(1960):1105–1118, 1997.

[67] J. Zhang, H. Chen, Y. Liu, H. Elledge, C. Mashuga, and S. Mannan. Dust Explosion of Carbon Nanofibers Promoted by Iron Nanoparticles. *Industrial & Engineering Chemistry Research*, 54(15):3989–3995, 2015.